Chapter 14

Structure of Polycrystalline Aggregates

14-1 INTRODUCTION

The normal way in which metals ceramics and other crystalline materials are produced and used is in the form of polycrystalline aggregates, composed of a great many individual crystals usually of microscopic size. Because the properties of such aggregates are of great technological importance, they have been intensively studied in many ways. In such studies the two most useful techniques are microscopic examination and x-ray diffraction, and the wise investigator will use them both; one complements the other, and both together can provide a great deal of information about the structure of an aggregate.

The properties (mechanical, electrical, chemical, etc.) of a single-phase aggregate are determined by two factors:

1) the properties of a single crystal of the material, and
2) the way in which the single crystals are put together to form the composite mass.

In this chapter the focus in on the second factor, namely, the *structure* of the aggregate, using this term in its broadest sense to mean the relative size, quality, and orientation of the grains making up the aggregate. Whether these grains are large or small, strained or unstrained, oriented at random or in some particular way, frequently has very important effects on the properties of the material.

If the aggregate contains more than one phase, its properties naturally depend on the properties of each phase considered separately and on the way these phases occur in the aggregate. Such a material offers wide structural possibilities since,

in general, the size, quality, and orientation of the grains of one phase may differ from those of the other phase or phases.

This chapter is divided into two parts. The first covers crystal size and crystal quality and the techniques for separating these contributions to line broadening. The second part deals with the orientation of the crystals within solids, i.e., with texture; techniques for texture qualification are covered.

CRYSTAL SIZE AND QUALITY

14-2 GRAIN SIZE

The size of the grains in a polycrystalline material has pronounced effects on many of its properties, the best known being the increase in strength and hardness of a metal or alloy which accompanies a decrease in grain size. This dependence of properties on grain size makes the measurement of grain size a matter of some importance in the control of most metal forming operations.

The grain sizes encountered in engineering materials range from about 1000 to 1 μm. These limits are, of course, arbitrary and represent rather extreme values; typical values fall into a much narrower range, namely, about 100 to 10 μm. The most accurate method of measuring grain size in this range is by microscopic examination; the usual procedure is to determine the average number of grains per unit area of the polished section and report this in terms of an "index number" established by ASTM. The equation

$$n = 2^{N-1}$$

relates n, the number of grains per square inch when viewed at a magnification of 100 ×, and N, the ASTM "index number" or "grain-size number." Grain-size numbers of 4 and 8, for example, correspond to grain diameters of 90 and 22 μm, respectively.

Although x-ray diffraction is decidedly inferior to microscopic examination in the accurate measurement of grain size, one diffraction photograph[1] can yield semiquantitative information about grain size, *together with* information about crystal quality and orientation. A transmission or back-reflection pinhole photograph made with filtered radiation is often used, but a focussing monochromator placed between the x-ray tube and the sample can also be used. If the back-reflection method is used, the surface of the specimen (which need not be polished) should be etched to remove any disturbed surface layer which might be present, because most of the diffracted radiation originates in a thin surface layer (see Secs. 14-4 and 14-5).

[1] In this context "photograph" can mean a two-dimensional diffraction pattern recorded on a photographic emulsion, a two-dimensional wire detector, a CCD (charge-coupled device) camera or an image plate. The advantages and disadvantages of each type of detector are summarized in Sec 6-10 and 7-4.

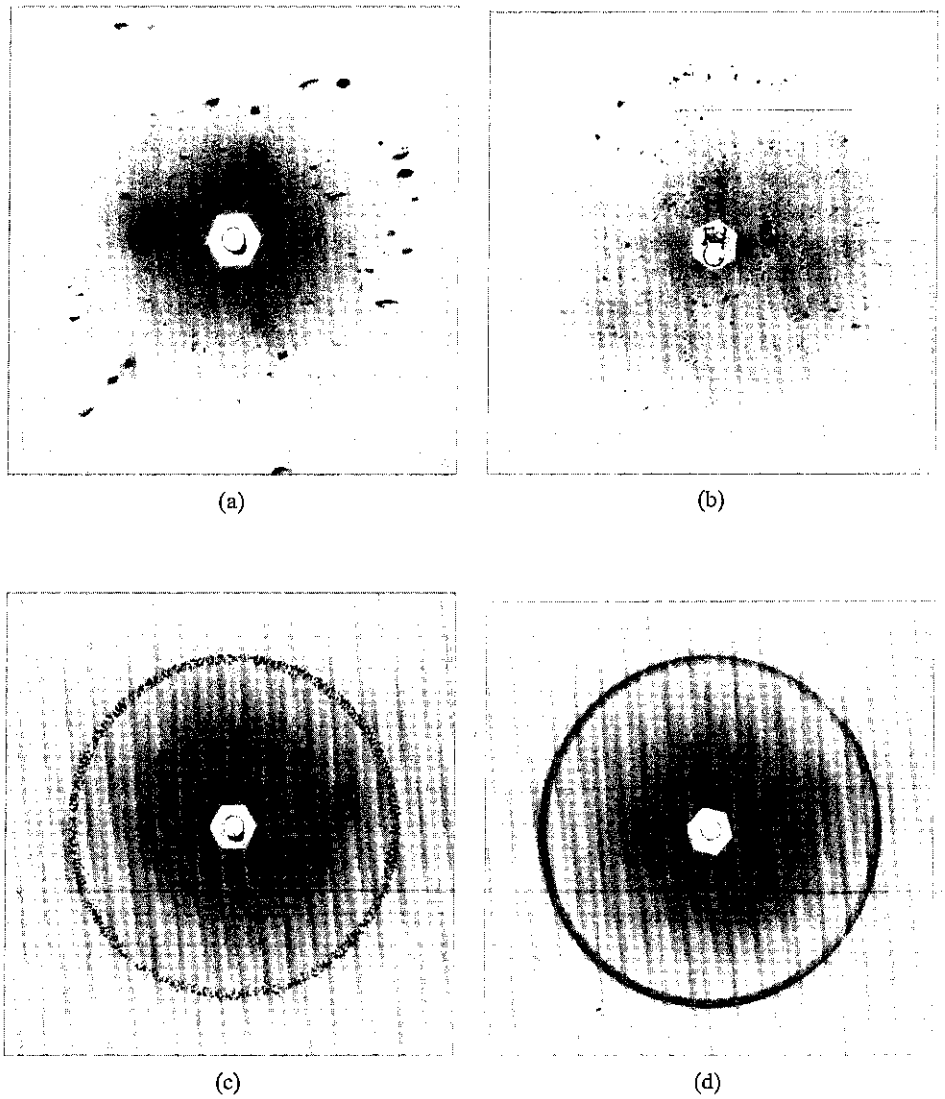

Figure 14-1 Back-reflection pinhole patterns of recrystallized aluminum specimens; grain size decreases in the order (a), (b), (c), (d). Filtered copper radiation.

The nature of the changes produced in pinhole photographs by progressive reductions in specimen grain size is illustrated in Fig. 14-1. The governing effect here is the number of grains which take part in diffraction. This number is in turn related to the cross-sectional area of the incident beam, and its depth of penetration (in back reflection) or the specimen thickness (in transmission). When the grain size is quite coarse, as in Fig. 14-1(a), only a few crystals diffract and the photograph consists of a set of superimposed Laue patterns, one from each crystal, due

to the white radiation present. A somewhat finer grain size increases the number of Laue spots, and those which lie on potential Debye rings generally are more intense than the remainder, because they are formed by the strong characteristic component of the incident radiation. Thus, the suggestion of Debye rings begins to appear, as in (b). When the grain size is further reduced, the Laue spots merge into a general background and only Debye rings are visible, as in (c). These rings are spotty, however, since not enough crystals are present in the irradiated volume of the specimen to reflect to all parts of the ring. A still finer grain size produces the smooth, continuous Debye rings shown in (d).

Several methods have been proposed for the estimation of grain size purely in terms of various geometrical factors. For example, an equation may be derived which relates the observed number of spots on a Debye ring to the grain size and other such variables as incident-beam diameter, multiplicity of the reflection, and specimen-film distance. However, many approximations are involved and the resulting equation is not very accurate. The best way to estimate grain size by diffraction is to obtain a set of specimens having known ASTM grain-size numbers, and to prepare from these a standard set of photographs of the kind shown in Fig. 14-1. The grain-size number of an unknown specimen of the same material is then obtained simply by matching its diffraction pattern with one of the standard photographs, *provided both are made under identical conditions.*

When the grain size reaches a value somewhere in the range 10 to 1 μm, the exact value depending on experimental conditions, the Debye rings lose their spotty character and become continuous. Between this value and 0.1 μm (1000 Å), no change occurs in the diffraction pattern. At about 0.1 μm the first signs of line broadening, due to small crystal size, begin to be detectable. There is therefore a size range, from 10 (or 1) to 0.1 μm, where x-ray diffraction is quite insensitive to variations in grain size, at least for an incident beam of normal size. With microbeam techniques, x-ray lines remain spotty down to smaller grain sizes than are mentioned above, allowing spots from individual grains to be observed and counted [7.10].

14-3 CRYSTALLITE SIZE

When the size of the individual crystals is less than about 0.1 μm (1000 Å), the term "particle size" is usually used, but the term "crystallite size" is more precise. As was demonstated in Sec. 5-2, crystals in this size range cause broadening of the Debye rings, the extent of the broadening being given by:

$$B = \frac{0.9\lambda}{t \cos \theta} \tag{5-2}$$

where B = FWHM (full width at half maximum) of the broadened diffraction line on the 2θ scale (radians) and t = diameter of the crystallites. All diffraction lines have a measurable breadth, even when the crystallite size exceeds 1000 Å, due to

such causes as divergence of the incident beam and size of the sample (in Debye cameras) and width of the x-ray source (in diffractometers). The breadth B in Eq. (5-2) refers, however, to the *extra* breadth, or broadening, due to the crystallite-size effect alone. In other words, B is essentially zero when the crystallite size exceeds about 1000 Å.

Some investigators prefer to determine the *integral breadth* of a diffraction line rather than the FWHM. The integral breadth is given by the integrated intensity divided by the maximum intensity, i.e., it is the width of a rectangle having the same area and height as the observed line.

The experimental difficulties involved in measuring crystallite size from line broadening increase with the size of the crystallite measured. Roughly speaking, relatively crude measurements suffice in the range 0-500 Å, but very good experimental technique is needed in the range 500-1000 Å. With the diffractometer, the upper limit can approach 2000 Å. Very careful work is required and back-reflection lines are employed, since such lines exhibit the largest crystallite-size broadening, as shown by Eq. (5-2).

Application of Eq. (5-2) to loose powders is straight-forward, but applying it to the broadened diffraction lines from very fine-grained metal specimens so as to determine the size of the individual grains is not very reliable. The individual grains of such a material are often nonuniformly strained, and this can also broaden the diffraction lines; an uncertainty therefore exists as to the exact cause of the observed broadening. On the other hand, the individual crystals which make up a loose powder of fine particle size can often be assumed to be strain-free, provided the material involved is a brittle (nonplastic) one and all the observed broadening can be ascribed confidently to the crystallite size effects. In such powders, the individual crystallites may be much smaller than the particle size since agglomeration of crystallites often occurs. (But note that loose, unannealed *metal* powders, produced by filing, grinding, ball milling, etc., almost always contain nonuniform strain.) Scherrer's equation, Eq (5-2) has been applied to the measurement of the crystallite size of such materials as carbon blacks, catalysts, and industrial dusts.

Figure 14-2 shows diffractometer scans (top) of a nanocrystalline composite consisting of a very small concentration of platinum nanocrystals in a matrix of amorphous carbon [14.1] and (bottom) of a poly crystalline sheet of platinum. A summary of data from this scan appears in Table 14-1, and the consistent crystallite size determined for each peak, as will be seen in Sec. 14-5, indicates that crystallite size is the major contribution to broadening in this sample.

Another x-ray method of measuring the size of small particles deserves some mention, although a complete description is beyond the scope of this book. This is the method of *small-angle scattering*. It is a form of diffuse scattering very near the undeviated transmitted beam, i.e., at angles 2θ ranging from 0° up to roughly 2 or 3°. From the observed variation of the scattered intensity vs. angle 2θ, the size, and to some extent the shape, of small particles can be determined, whether they are amorphous or crystalline [G.34, G.35, 14.2]. Small-angle scattering has also been

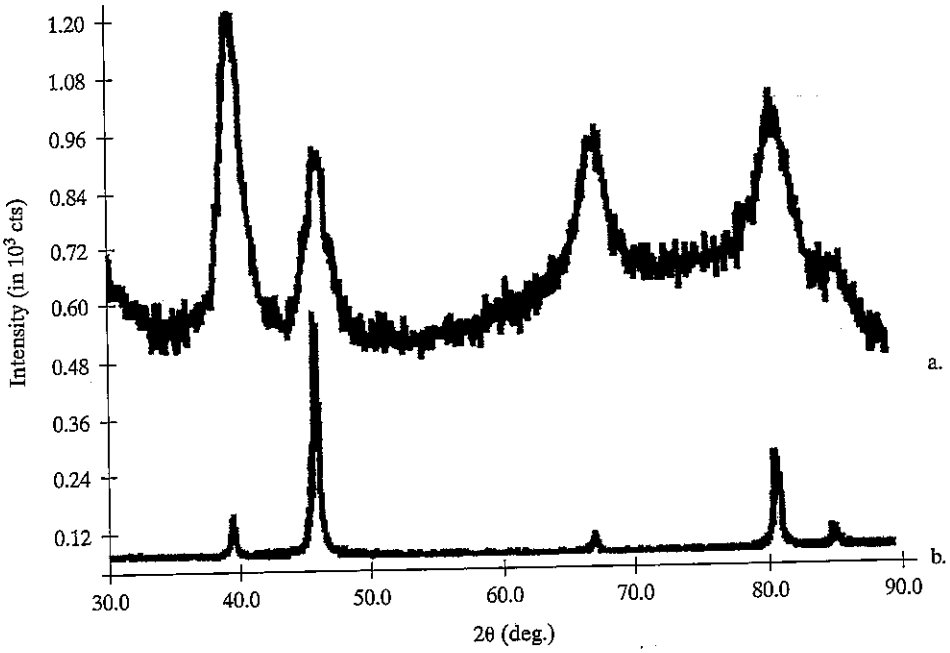

Figure 14-2 Comparison of θ-2θ diffraction patterns for platinum nanoparticles in a silica matrix [14.1] (top) and rolled platinum sheet showing strong preferred orientation (bottom).

TABLE 14.1

hkl	FWHM (°2θ)	t (Å)
111	1.9	50
200	1.7	55
220	2.1	50
311	2.5	45-50

used to study precipitation effects in metallic solid solutions. Chapter 19 provides a brief introduction to small angle scattering.

14-4 CRYSTAL QUALITY (MICROSTRAIN)

Nonuniform strain is characteristic of the *cold-worked state* of metals and alloys and has been observed in ceramics and semiconductors. When a polycrystalline piece of metal is plastically deformed, for example by rolling, slip occurs in each grain and the grain changes its shape, becoming flattened and elongated in the direction of rolling. The change in shape of any one grain is determined not only by the forces applied to the piece as a whole, but also by the fact that each grain retains

contact on its boundary surfaces with all its neighbors. Because of this interaction between grains, a single grain in a polycrystalline mass is not free to deform in the same way as an isolated crystal would, if subjected to the same deformation by rolling. As a result of this constraint by its neighbors, a plastically deformed grain in a solid aggregate usually has regions of its lattice left in an elastically bent or twisted condition or, more rarely, in a state of uniform tension or compression. The metal is then said to contain *residual stress*. (Such stress is often called "internal stress" but the term is not very informative since all stresses, residual or externally imposed, are internal. The term "residual stress" emphasizes the fact that the stress remains after all external forces are removed.)

When an annealed metal or alloy is cold worked, its diffraction lines become broader. This is a well-established, easily verified experimental fact, but its explanation was for many years a matter of controversy. Some investigators felt that the chief effect of cold work was to fragment the grains to a point where their small size alone was sufficient to account for all the observed broadening. Others concluded that the nonuniformity of strain produced by cold work was the major cause of broadening, with grain fragmentation possibly a minor contributing cause. This controversy revolved around the measurement of line widths and their interpretation in terms of either "particle-size broadening," according to Eq. (5-2), or "strain broadening," Eq. (5-9).

In 1949, however, Warren pointed out that there was important information about the state of a cold-worked metal in the *shape* of its diffraction lines, and that to base conclusions only on line *width* was to use only part of the experimental evidence. If the observed line profiles, corrected for instrumental broadening, are expressed as Fourier series, then an analysis of the Fourier coefficients discloses both particle size and strain, without the necessity for any prior assumption as to the existence of either [4.3, G.17, G.20]. Warren and Averbach [14.4] made the first measurements of this kind, on brass filings, and many similar studies followed [14.5]. Somewhat later, Paterson [14.6] showed that the Fourier coefficients of the line profile could also disclose the presence of stacking faults caused by cold work. (In FCC metals and alloys, for example, slip on {111} planes can here and there alter the normal stacking sequence *ABCABC* ... of these planes to the faulted sequence *ABCBCA* ....) Thus three causes of line broadening are now recognized: small crystallite size, nonuniform strain, and stacking faults.

These studies of line shape showed that it was impossible to generalize about the causes of line broadening in cold-worked metals and alloys. In some materials all three causes contribute, in others only one.

The broadening of a diffraction line by deformation cannot always be observed by simple inspection of a photograph or a diffractometer scan unless some standard is available for comparison. However, the separation of the $K\alpha$ doublet furnishes a very good "internal standard." In the back-reflection region, a relatively strain-free material produces a well-resolved doublet, one component due to $K\alpha_1$ radiation and the other to $K\alpha_2$. For a given set of experimental conditions, the separation of this doublet is constant and independent of the amount of microstrain. But as the

amount of deformation is increased, the broadening increases, until finally the two components of the doublet overlap to such an extent that they appear as one unresolved line. An unresolved $K\alpha$ doublet can therefore be taken as evidence of cold work, if the same doublet is resolved when the material is in the annealed or strain-free condition.

With this background, consider some of the diffraction effects associated with the processes of *recovery, recrystallization*, and *grain growth*. When a cold-worked metal or alloy is annealed at a low temperature, recovery takes place; at a somewhat higher temperature, recrystallization; and at a still higher temperature, grain growth. Or at a sufficiently high constant temperature, these processes may be regarded as occurring consecutively in time. During recovery, both macro- and micro-residual stress are reduced in magnitude, but strength and hardness remain high; much of this stress relief appears to be due to polygonization, which can occur in the individual grains of an aggregate just as in a single crystal. During recrystallization, new grains form, residual stress is practically eliminated, and strength and hardness decrease rather abruptly. During grain growth some grains grow larger by swallowing neighboring grains.

Because the nonuniform strain due to residual microstress is the major cause of deformation-induced line broadening, the broad diffraction lines characteristic of cold-worked metal partially sharpen during recovery. When recrystallization occurs, the lines attain their maximum sharpness. During grain growth, the lines become increasingly spotty as the grain size increases.

The hardness curve and diffraction patterns of Fig. 14-3 illustrate these changes for an alpha brass, a solid solution of zinc in copper, containing 30 percent zinc by weight. The hardness remains practically constant, for an annealing period of one hour, until a temperature of 200°C is exceeded, and then decreases rapidly with increasing temperature, as shown in (a). The diffraction pattern in (b) exhibits the broad diffuse Debye lines produced by the cold-rolled, unannealed alloy. These lines become somewhat narrower for specimens annealed at 100° and 200°C, and the $K\alpha$ doublet becomes partially resolved at 250°C. At 250°C, therefore, the recovery process appears to be substantially complete in one hour and recrystallization is just beginning, as evidenced by the drop in Rockwell B hardness from 98 to 90. At 300°C the diffraction lines are quite sharp, and the doublets are completely resolved, as shown in (c). Annealing at temperatures above 300°C causes the lines to become increasingly spotty, indicating that the newly recrystallized grains are increasing in size. The pattern of a specimen annealed at 450°C, when the hardness had dropped to 37 Rockwell B, appears in (d).

Diffractometer measurements made on the same specimens disclose both more, and less, information. Some automatically recorded profiles of the 331 line, the outer ring of the patterns shown in Fig. 14-3, are reproduced in Fig. 14-4. It is much easier to follow changes in line shape by means of these curves than by inspection of pinhole photographs. Thus the slight sharpening of the line at 200°C is clearly evident in the diffractometer record, and so is the doublet resolution which occurs at 250°C. But note that the diffractometer cannot "see" the spotty diffraction lines

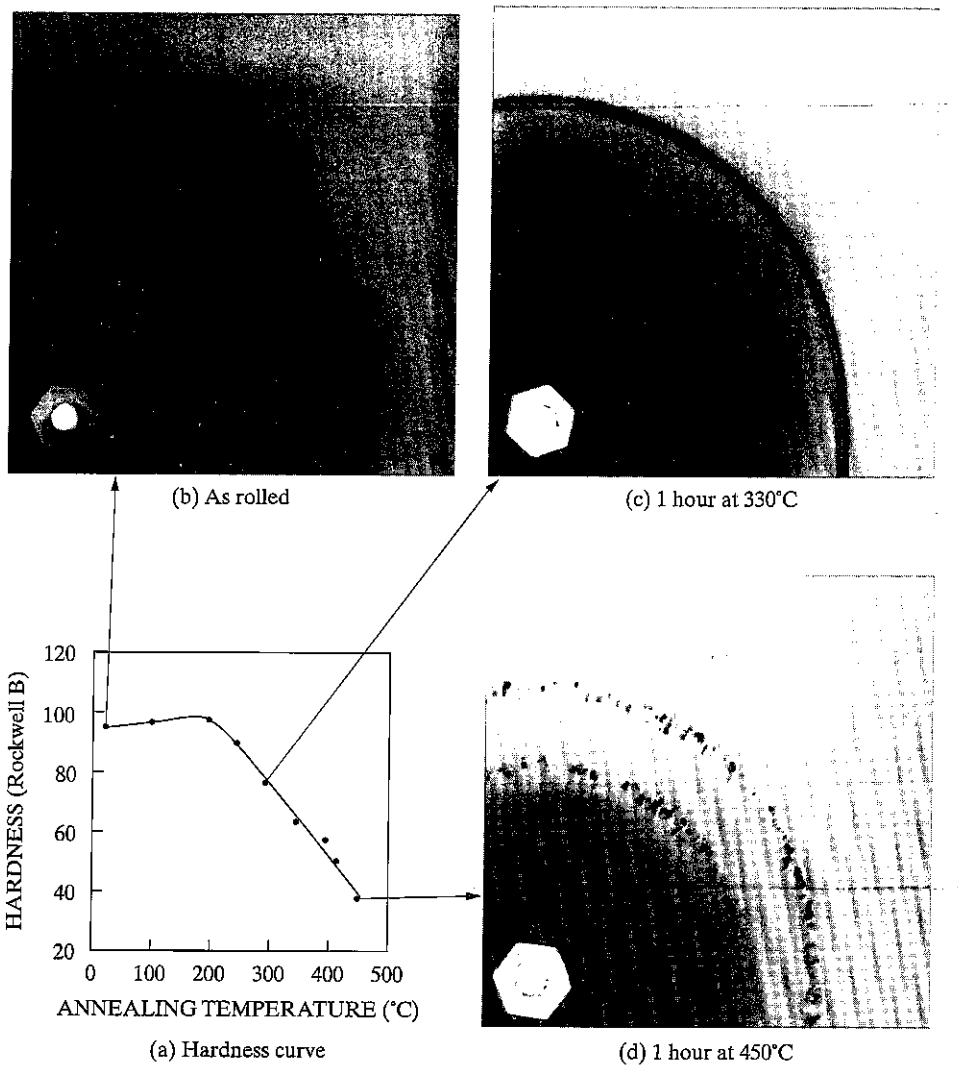

Figure 14-3 Changes in hardness and diffraction lines of 70 Cu-30 Zn specimens, reduced in thickness by 90 percent by cold rolling, and annealed for 1 hour at the temperatures indicated in (a), (b), (c), and (d) are portions of back-reflection pinhole patterns of specimens annealed at the temperatures stated (filtered copper radiation).

caused by coarse grains. There is nothing in the diffractometer records made at 300° and 450°C which would immediately suggest that the specimen annealed at 450°C had the coarser grain size, but this fact is quite evident in the pinhole patterns shown in Figs. 14-3(c) and (d).

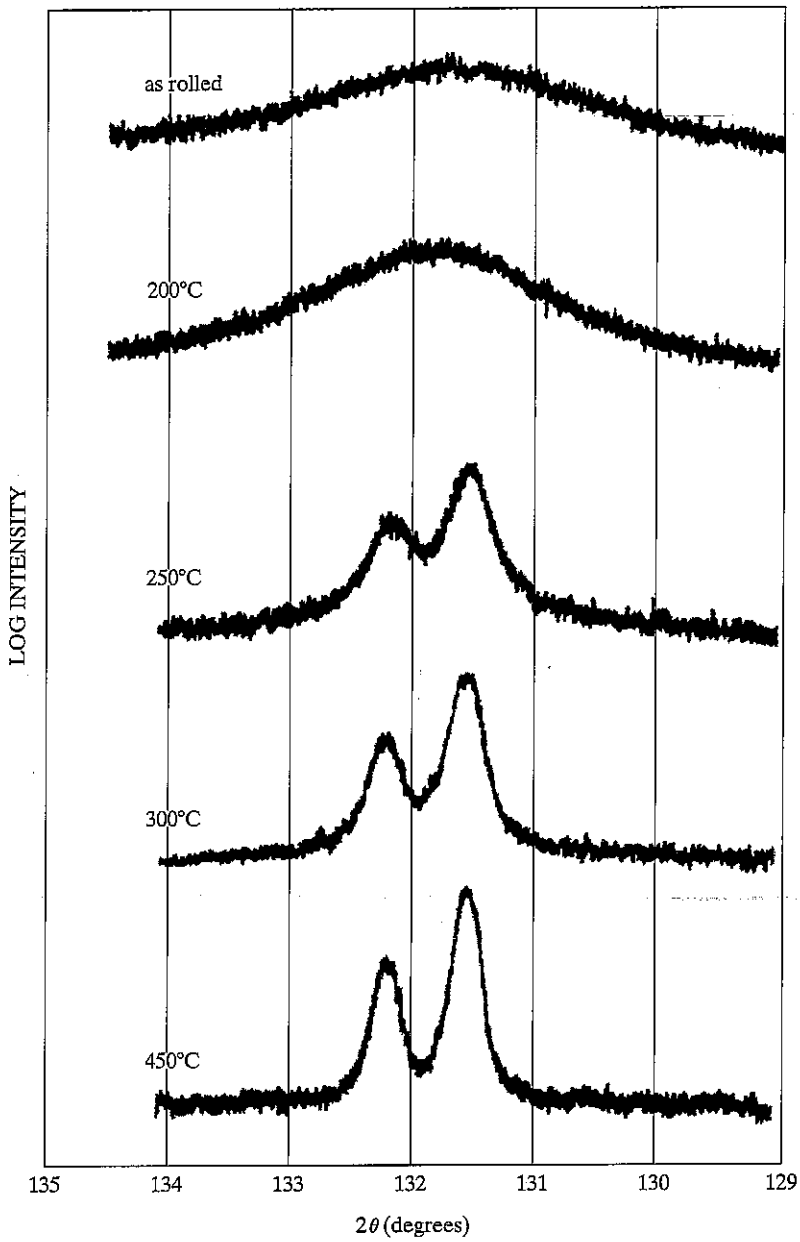

Figure 14-4 Diffractometer traces of the 331 line of the cold-rolled and annealed 70-30 brass specimens described in Fig.14-3. Filtered copper radiation. Logarithmic intensity scale. All curves displaced vertically by arbitrary amounts.

If an x-ray camera or two-dimensional detector are not available, a piece of dental film can be placed just in front of the detector slit of the diffractometer can disclose whether or not the diffraction lines are spotty. (Dental x-ray film, available from dental supply houses, comes in the form of a single piece of film, typically about 4 × 5 cm, enclosed in a thin envelope of light-tight plastic.[2]) If a diffraction line is spotty on a photograph, the grain size of the specimen is too large for accurate intensity measurements with the diffractometer.

Figures 14-3 and 14-4 illustrate line sharpening by annealing. Conversely, when an annealed metal is progressively deformed, the x-ray lines progressively broaden and the hardness increases. In fact, the hardness of a particular metal or alloy can be rather accurately measured from the breadth of its diffraction lines. The relation between line breadth and hardness is not general, but must be determined experimentally for each particular material. (Very slight degrees of deformation can be detected by observation of the $K\alpha$ doublet. Rather than attempting to measure a slight increase in line width, one measures the ratio of the height of the "valley" between $K\alpha_1$ and $K\alpha_2$ to the height of $K\alpha_2$. This ratio increases rapidly as the lines broaden.)

When steel is hardened by quenching, the x-ray lines become very broad because of the microstrains due to the formation of martensite. Subsequent tempering causes progressive softening and line sharpening. Here again, a useful relation can be established experimentally between line width and hardness, applicable to a particular type of steel.

Line-width observations are often made in back reflection, whether by a photographic technique (Fig. 14-3) or by the diffractometer (Fig. 14-4). It is then necessary to remember that the observation applies only to a thin surface layer of the specimen. For example, Fig. 14-5(a) was obtained from a piece of copper and exhibits unresolved doublets in the high-angle region. The inexperienced observer might conclude that this material was highly cold worked. What the x-ray "sees" *is* cold worked, but it sees only to a limited depth. Actually, the bulk of this specimen is in the annealed condition, but the surface from which the x-ray pattern was made had had 50 μm removed by grinding on a belt sander after annealing. This treatment cold worked the surface to a considerable depth. By successive etching treatments and diffraction patterns made after each etch, the change in structure of the cold-worked layer could be followed as a function of depth below the ground surface. Not until a total of 75 μm had been removed did the diffraction pattern become characteristic of the bulk of the material; see Fig. 14.5(b), where the spotty lines indicate a coarse-grained, recrystallized structure.

[2] Even if no photographic work is done in the x-ray laboratory in which one is working, and hence no developing and fixing solutions are on hand, it is possible to use a small amount of developer and fixer from a TEM darkroom or from a darkroom for printing positives from microscopy negatives.

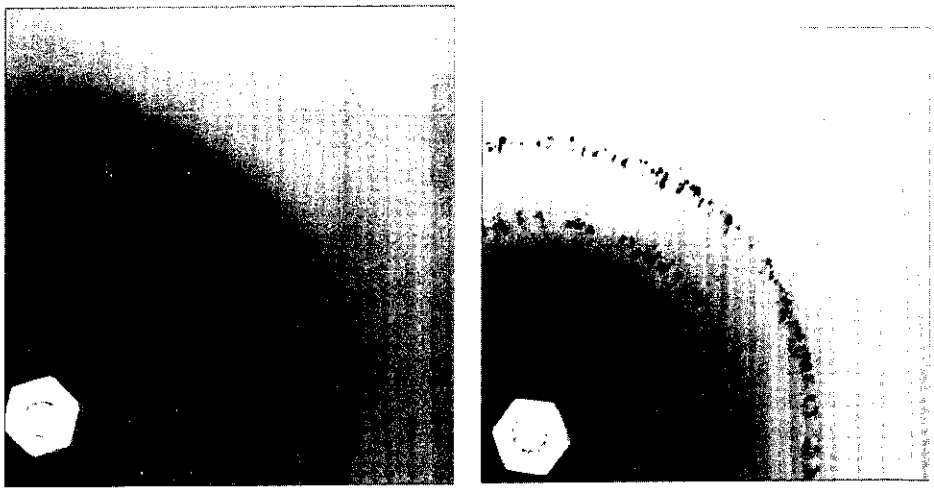

(a) (b)

Figure 14-5 Back-reflection pinhole patterns of coarse-grained recrystallized copper. Unfiltered copper radiation: (a) from surface ground on a belt sander; (b) after removal of 0.003 in. (75 μm) from this surface by etching.

14-5 DEPTH OF X-RAY PENETRATION

Observations of this kind suggest that it might be well to consider in some detail the general problem of x-ray penetration. Most metallurgical specimens strongly absorb x-rays, and the intensity of the incident beam is reduced almost to zero in a very short distance below the surface. The diffracted beams therefore originate chiefly in a thin surface layer whenever a reflection technique, as opposed to a transmission technique, is used, i.e., whenever a diffraction pattern is obtained in a back-reflection camera of any kind, a Seemann-Bohlin camera, or a diffractometer as normally used. The example of Fig. 14-5 just showed how a back-reflection pinhole photograph of a ground surface discloses the cold-worked condition of a thin surface layer and gives no information whatever about the bulk of the material below that layer.

These circumstances naturally pose the following question: what is the effective depth of x-ray penetration? Or, stated in a more useful manner, to what depth of the specimen does the information in such a diffraction pattern apply? This question has no precise answer because the intensity of the incident beam does not suddenly become zero at any one depth but rather decreases exponentially with distance below the surface. Building on the results of Sec 4-10, one can express the intensity diffracted by the layer at depth α as a fraction of the total integrated intensity diffracted by a specimen of infinite thickness (a few thousandths of an inch for most metals). Call this fraction G_x. Then

$$G_x = \frac{\int_{x=0}^{x=x} dI_D}{\int_{x=0}^{x=\infty} dI_D} = [1 - e^{-\mu x(1/\sin\gamma + 1/\sin\beta)}] \qquad (14\text{-}3)$$

permits calculatation of the fraction G_x of the total diffracted intensity which is contributed by a surface layer of depth x. Suppose that a contribution from this surface layer of 95 percent (or 99 or 99.9 percent) of the total is enough so that the contribution from the material below that layer can be ignored then x is the effective depth of penetration. The information recorded on the diffraction pattern (or, more precisely, 95 percent of the information) then refers to the layer of depth x and not to the material below it. As was seen before for the parafocusing diffractometer, $\gamma = \beta = \theta$, and Eq. (14-3) reduces to

$$G_x = (1 - e^{-2\mu x/\sin\theta}), \qquad (14\text{-}4)$$

which shows that the effective depth of penetration decreases as θ decreases and therefore varies from one diffraction line to another. In back-reflection cameras, $\gamma = 90°$, and

$$G_x = [1 - e^{-\mu x(1+1/\sin\beta)}], \qquad (14\text{-}5)$$

where $\beta = 2\theta - 90°$.

For example, the conditions applicable to the outer diffraction ring of Fig. 14-5 are $\mu = 473\ \text{cm}^{-1}$ and $2\theta = 136.7°$. By using Eq. (14-5), G_x can be determined as function of x (Fig. 14-6). Note that 95 percent of the information on the diffraction pattern refers to a depth of only about 25 μm. It is therefore not surprising that the pattern of Fig. 14-5(a) discloses only the presence of cold-worked metal, since repeated etching treatments showed that the depth of the cold-worked layer was about 75 μm. Of course, the information recorded on the pattern is heavily weighted in terms of material just below the surface; thus 95 percent of the recorded information applies to a depth of 25 μm, but 50 percent of *that* information originates in the first 25 μm. (Note that an effective penetration of 25 μm means that a surface layer only one grain thick is effectively contributing to the diffraction pattern if the specimen has an ASTM grain-size number of 8. This layer contains some 300,000 reflecting lattice planes for the 331 diffraction line considered here.)

Equation (14-4) can be put into the following form, which is more suitable for calculation:

$$\frac{2\mu x}{\sin\theta} = ln\left(\frac{1}{1 - G_x}\right) = K_x,$$

$$x = \frac{K_x \sin\theta}{2\mu}. \qquad \text{[Diffractometer]}$$

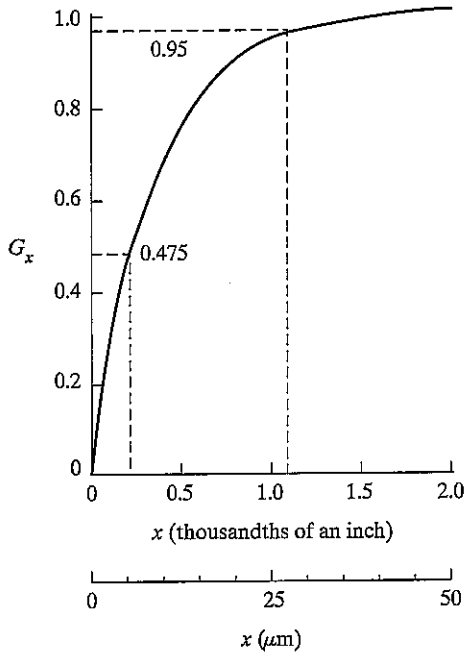

Figure 14-6 The fraction G_x of the total diffracted intensity contributed by a surface layer of depth x, for $\mu = 473\ \text{cm}^{-1}$, $2\theta = 136.7°$, and normal incidence.

Similarly, Eq. (14-5) becomes

$$\mu x\left(1 + \frac{1}{\sin\beta}\right) = ln\left(\frac{1}{1 - G_x}\right) = \mathrm{K_x},$$

$$x = \frac{K_x \sin\beta}{\mu(1 + \sin\beta)}. \quad \text{[Back-reflection camera]}$$

Values of K_x for various assumed values of G_x are given in Table 14-2.

Calculations of the effective depth of penetration can be valuable in many applications of x-ray diffraction. The effective depth of penetration must be made as large as possible in some applications. Then γ and β in Eq. (14-3) must be as large as possible, indicating the use of high-angle lines, and μ as small as possible, indicating short-wavelength radiation. Other applications may demand very little penetration, as when information, e.g., chemical composition or lattice parameter, is needed from a very thin surface layer. Then μ must be made large, by using radia-

TABLE 14.2

G_x	0.50	0.75	0.90	0.95	0.99	0.999
K_x	0.69	1.39	2.30	3.00	4.61	6.91

tion which is highly absorbed, and γ and β small, by using a diffractometer at low values of 2θ.[3] By these means the depth of penetration can often be made surprisingly small. For instance, if a steel specimen is examined in a diffractometer with Cu $K\alpha$ radiation, 95 percent of the information afforded by the lowest angle line of ferrite (the 110 line at $2\theta = 45°$) applies to a depth of only 2 μm. There are limits, of course, to reducing the depth of x-ray penetration, and when information is required from very thin surface films, electron diffraction, glancing angle diffraction, or x-ray reflectivity are far more suitable tools.

Although the diffracted beam in any reflection method comes only from a very thin surface layer, it must not be supposed that the information on a diffraction pattern obtained by a transmission method is truly representative of the entire cross section of the specimen. Calculations such as those given above show that a greater proportion of the total diffracted energy originates in a layer of given thickness on the back side of the specimen (the side from which the transmitted beam leaves) than in a layer of equal thickness on the front side. If the specimen is highly absorbing, a transmission method can be almost as nonrepresentative of the entire specimen as a back-reflection method, in that most of the diffracted energy will originate in a thin surface layer. See Problem 14-5.

14-6 SIZE AND STRAIN SEPARATION

As indicated in Sec. 14-4, separating the different contributions to line broadening, if present, requires use of multiple diffraction peaks and analysis of the peaks' shapes. The quality of the diffraction pattern, or more specifically the diffraction peaks and their tails, must be very high if the somewhat involved Fourier analysis pioneered by Warren is to be worthwhile [e.g., 14.3 - 14.6, Chap. 7 of 6.7, Chap. 9 of G.17, Chap. 13 of G.20, and Chap. 8 of G.35]. Other simpler approaches using peak widths have their place in analyzing size and strain broadening.

It is important to realize that crystallite sizes obtained from peak width measurements give volume-average sizes whereas those from peak shape analysis give number-averages. This can be seen by comparing a histogram of average crystallite diameters observed with TEM (Fig. 14-7) with the average diameter determined from diffractometry and the Scherrer equation (Eq. 5-2) [14.7]. The sample was a dilute mixture of platinum nanoparticles in an amorphous silica matrix, the diffraction pattern of the sample appears in Fig. 14-2 and Table 14-1 lists the crystallite sizes obtained from the x-ray diffraction peaks and Scherrer's equation. The crystallite size averaged 38 Å from TEM and 50 Å from the FWHM of the x-ray diffraction peaks. A small number of very large crystallites were noted during TEM of the samples, and simulation of the diffraction peaks [14.8] produced by a small number of large crystallites mixed with a much larger number of 35-40 Å crystal-

[3] Some of these requirements may be contradictory. For example, in measuring the lattice parameter of a thin surface layer with a diffractometer, a compromise must be found between the low value of θ required for shallow penetration and the high value of θ required for precise parameter measurements.

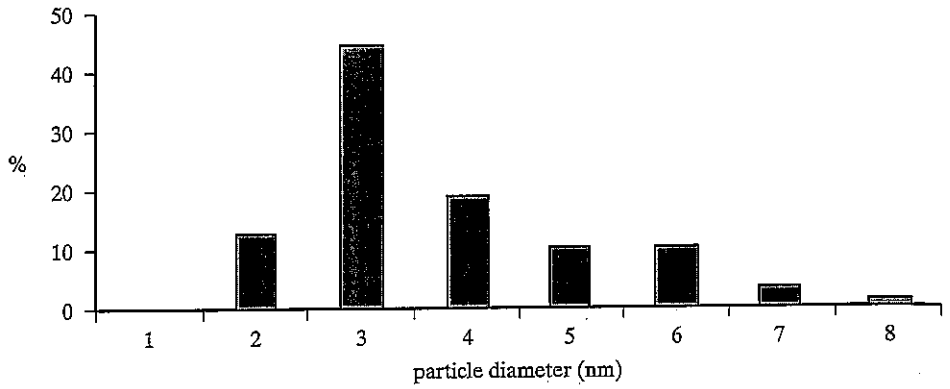

Figure 14-7 Histogram of Pt nanocluster size as observed by TEM in a Pt/silica xerogel nanocomposite [14.10].

lites reveals that this is the probable origin of the difference between TEM and X-ray FWHM sizes.

Contributions from crystallite size, micro strain and instrumental effects can be separated in a straight-forward fashion if the peaks are Lorentzian- or Gaussian-shaped. If

B_{exp} is the experimentally measured FWHM,
B_{size} is the FWHM due to crystallite size,
B_{strain} is the FWHM due to micro strain and
B_{inst} is the FWHM due to the instrument,

then for Lorentzian peaks

$$B_{exp} = B_{size} + B_{strain} + B_{inst} \tag{14-8}$$

and for Gaussian peaks

$$B^2_{exp} = B^2_{size} + B^2_{strain} + B^2_{inst}. \tag{14-9}$$

Correction for the instrumental width in either case can be obtained by recording a diffraction pattern, under identical conditions, of the same substance but in a well-annealed, large-grained condition.

Separation of size and strain components can be done by plotting $B \cos \theta$ as a function of $\sin \theta$ (Fig. 14-8); this type of plot is known as a Williamson-Hall plot [14.9] and implicitly assumes that peak shapes are Lorentzian. Rearranging the terms of Eq. 5-2 produces

$$B \cos \theta = 0.9\lambda/t \tag{14-10}$$

and of Eq. 5-9 yields

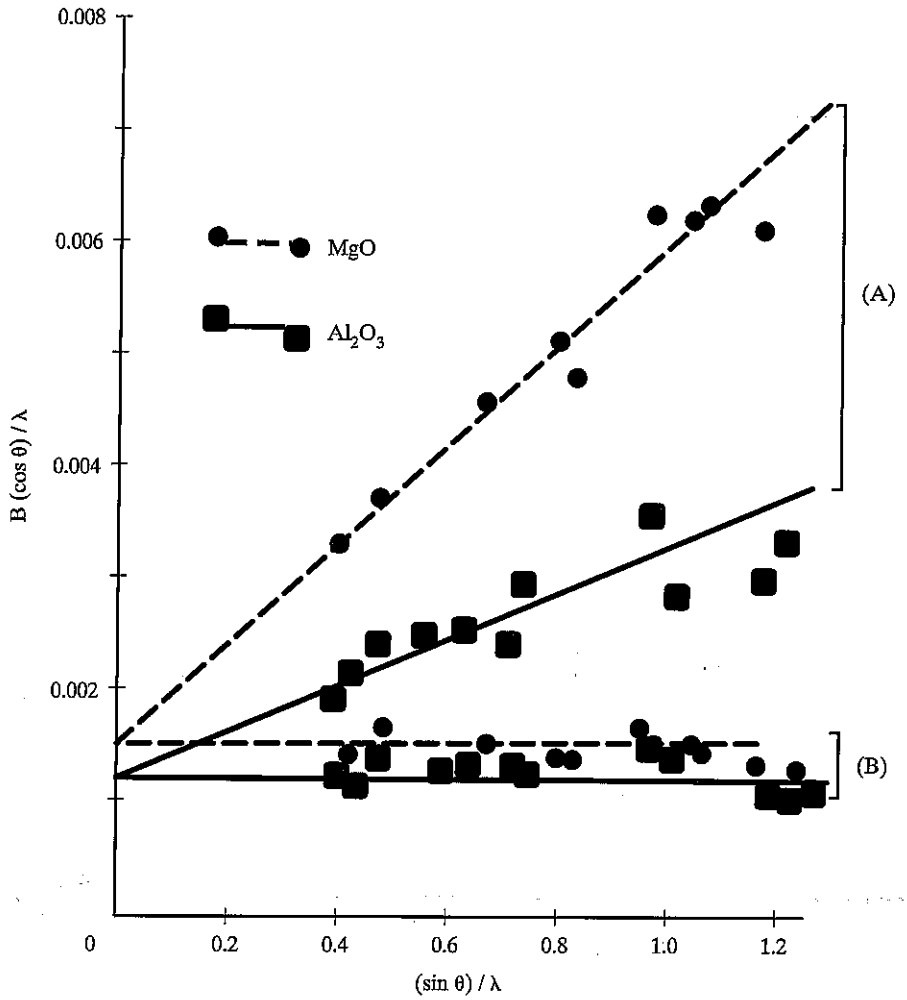

Figure 14-8 Williamson-Hall plot for MgO and Al_2O_3, curves (A) ball milled for 2 hours and (B) ball milled for 2 hours, then annealed for 2 hours at 1350° C. After Lewis and Lindley [14.10].

$$\beta \cos\theta = -2(\Delta d/d) \sin\theta. \tag{14-11}$$

If size broadening is the only significant contribution to peak width, then $B_{exp} \cos\theta$ is a constant for all peaks (i.e., its Williamson-Hall plot is a horizontal line). If strain broadening is the important contribution, $B_{exp} \cos\theta$ is a linear function of $\sin\theta$. Figure 14-8 shows data for two oxide ceramics in two conditions: after ball milling and ball milling followed by annealing at 1350 C for 2 hr [14.10]. As one would expect, ball milling produces less microstrain in Al_2O_3, a substance which is often used to polish solid samples prior to optical microscopy, and the crystallite size of

the two oxides is similar. The crystallite size remained constant after annealing, but virtually all of the strain was relieved.

CRYSTAL ORIENTATION

14-7 GENERAL

Each grain in a polycrystalline aggregate normally has a crystallographic orientation different from that of its neighbors. Considered as a whole, the orientations of all the grains may be randomly distributed in relation to some selected frame of reference, or they may tend to cluster, to a greater or lesser degree, about some particular orientation or orientations. Any aggregate characterized by the latter condition is said to have a *preferred orientation, or texture*, which may be defined simply as a condition in which the distribution of crystal orientations is nonrandom As discussed in Chap. 4 preferred orientation can have a profound effect on diffracted intensities measured by diffractometry.

Preferred orientation is a very common condition. Among metals and alloys it is most evident in wire and sheet, and the kinds of texture found in these products are treated below. The preferred orientation that is produced by the forming process itself (wire drawing or sheet rolling) is called a *deformation texture*. It is due to the tendency of the grains in a polycrystalline aggregate to rotate during plastic deformation; each grain undergoes slip and rotation in a complex way that is determined by the imposed forces and by the slip and rotation of adjoining grains; the result is a preferred, nonrandom orientation. When the cold-worked metal, possessed of a deformation texture, is recrystallized by annealing, the new grain structure usually has a preferred orientation too, often different from that of the cold-worked material. This is called a *recrystallization texture* or *annealing texture*. It is due to the influence which the texture of the cold-worked matrix has on the nucleation and/or growth of the new grains in that matrix.

Preferred orientation is not confined to metallurgical products. It also exists in rocks, in ceramics, in semiconductor thin films and other coatings and in both natural and artificial polymeric fibers and sheets. In fact, preferred orientation is generally the rule, not the exception, and the preparation of an aggregate with completely random crystal orientations is a difficult matter.

The industrial importance of preferred orientation lies in the effect, often very marked, which it has on the overall, macroscopic properties of materials. Given the fact that all single crystals are anisotropic, i.e., have different properties in different directions, it follows that an aggregate having preferred orientation must also have directional properties to a greater or lesser degree. Such properties may or may not be beneficial, depending on the intended use of the material. For example, sheet steel for the cores of small electric motors should have, for magnetic reasons, all grains oriented with their {100} planes parallel to the sheet surface. But this texture would not be satisfactory if the steel were to be formed into a cup by deep drawing: here a texture with {111} planes parallel to the surface would make the steel less

likely to crack during the severe deformation of deep drawing; however, if the part to be formed by deep drawing has an unsymmetrical shape, a still different texture, or none at all, might yield better results. Some control of texture is possible by the proper choice of production variables such as degree of deformation and annealing temperature, but metallurgists do not yet understand texture formation well enough to produce any desired texture in any particular metal at will.

Because of its technological importance, the literature on observed textures and an texture prediction is extensive. For information on deformation and recrystallization textures observed in specific materials in wire and sheet form, the reader should consult Barrett and Massalski [G.10] and Dillamore and Roberts [14.11]. Here the focus is on the nature of textures and with their determination by x-ray methods. Detailed coverage of the various techniques, special experimental methods and computational techniques appears elsewhere [G.36 and G.37].

As was noted before in this book, a pinhole photograph made of a polycrystalline specimen with characteristic radiation consists of concentric Debye rings. The implicit assumption has been that these rings are always continuous and of constant intensity around their circumference, but actually such rings are not formed unless the individual crystals in the specimen have completely random orientations.[4] If the specimen exhibits preferred orientation, the Debye rings are of nonuniform intensity around their circumference (if the preferred orientation is slight), or actually discontinuous (if there is a high degree of preferred orientation). In the latter case, certain portions of the Debye ring are missing because the orientations which would diffract to those parts of the ring are simply not present in the specimen. Nonuniform Debye rings can therefore be taken as conclusive evidence for preferred orientation, and analyzing the nonuniformity allows determination of the kind and degree of preferred orientation present. (This nonuniformity is evident even in some Hull/Debye–Scherrer patterns: if a wire having preferred orientation is examined in a Hull/Debye–Scherrer camera, the nonuniformity of Debye rings is usually apparent even though such a camera records only a portion of the rings.)

Fiber Texture

The individual crystals in wire are so oriented that the same crystallographic direction [*uvw*] in most of the grains is parallel or nearly parallel to the wire axis. Because a similar texture occurs in natural and artificial fibers, it is called a *fiber texture* and the axis of the wire is called the *fiber axis*. Materials having a fiber texture have rotational symmetry about an axis: all crystal orientations about this axis are equally probable, like those of beads on a string. A fiber texture is therefore to be expected in any material formed by forces that have rotational symmetry about an axis, for example, in wire and rod formed by drawing, swaging, or extrusion. Less common examples of fiber texture are sometimes found in sheet formed by simple

[4] See the next section for one exception to this statement.

compression, in coatings formed by hot dipping, electroplating, and evaporation, and in castings among the columnar crystals next to the mold wall. The fiber axis in these is perpendicular to the plane of the sheet or coating, and parallel to the axis of the columnar crystals.

Fiber textures vary in perfection, i.e., in the scatter of the direction [*uvw*] about the fiber axis, and both single and double fiber textures have been observed. Thus, cold-drawn aluminum wire has almost a single [111] texture, but copper, also FCC, has a double [111] + [100] texture; i.e., in drawn copper wire there are two sets of grains, the fiber axis of one set being [111] and that of the other set [100].

Sheet Texture

In its simplest, most highly developed form, the texture of sheet is such that most of the grains are oriented with a certain crystallographic plane (*hkl*) roughly parallel to the sheet surface, and a certain direction [*uvw*] in that plane roughly parallel to the direction in which the sheet was rolled. Such a texture is described by the shorthand notation (*hkl*)[*uvw*]. In an ideal texture of this kind, the grain orientations in the sheet are fixed with respect to axes in the sheet; there is none of the rotational freedom of grain orientation possessed by a fiber texture.

The notation (*hkl*)[*uvw*] specifies what is called an *ideal orientation*. Some metals and alloys have sheet textures so sharp that they can be adequately described by stating the ideal orientation to which the grains of the sheet closely conform. Most sheet textures, however, have so much scatter that they can be approximated symbolically only by the sum of a number of ideal orientations or texture components, and even such a description is inadequate. Thus, the deformation texture of brass sheet (70 Cu-30 Zn) is very near the ideal orientation (110)[$\bar{1}$12]. But both the deformation and recrystallization textures of low-carbon sheet steel have so much scatter that the grain orientations present can be represented accurately only by a graphical description, such as a *pole figure*.

Pole Figures

A pole figure is a stereographic projection, with a specified orientation relative to the specimen, that shows the variation of pole density with pole orientation for a selected set of crystal planes. This method of describing textures was first used by the German metallurgist Wever in 1924 [14.12], and its meaning can best be illustrated by the following example. Suppose a very coarse-grained sheet of a cubic metal contains only 10 grains, and the orientation of each of these 10 grains has been determined by one of the Laue methods. The orientations of all of these grains can be summarized by plotting the positions of their {100} poles on a single stereographic projection, with the projection plane parallel to the sheet surface. Since each grain has three {100} poles, there will be a total of $3 \times 10 = 30$ poles plotted on the projection. If the grains have a completely random orientation, these poles

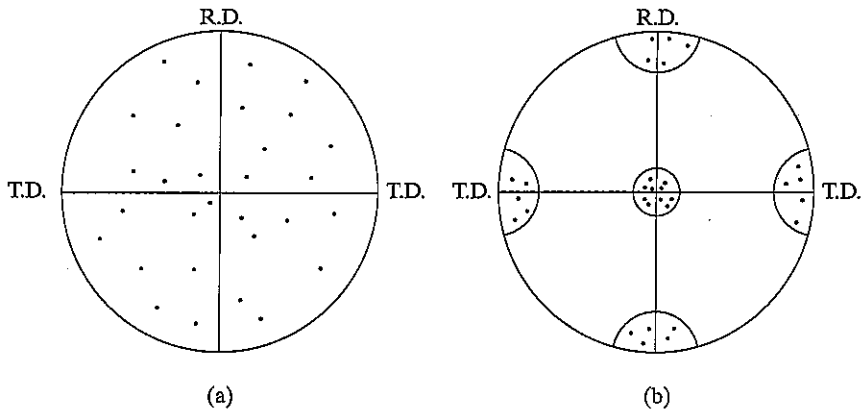

Figure 14-9 (100) pole figures for sheet material, illustrating (a) random orientation and (b) preferred orientation. R.D. (rolling direction) and T.D. (transverse direction) are reference directions in the plane of the sheet.

will be distributed uniformly[5] over the projection, as indicated in Fig. 14-9(a). But if preferred orientation is present, the poles will tend to cluster is certain areas of the projection, leaving other areas virtually unoccupied. For example, this clustering might take the particular form shown in Fig. 14-9(b). This is called the "cube texture," because each grain is oriented with its (100) planes nearly parallel to the sheet surface and the [001] direction in these planes nearly parallel to the rolling direction. (This simple texture, which may be described by the shorthand notation (100)[001], actually forms as a recrystallization texture in many face-centered cubic metals and alloys under suitable conditions.) If a (111) pole figure were constructed by plotting only {111} poles, the resulting pole figure would look entirely different from Fig. 14-9(b) for the same preferred orientation; in fact, it would consist of four "high-intensity" areas, one near the center of each quadrant. This illustrates the fact that the appearance of a pole figure depends on the indices of the poles plotted, and that the choice of indices depends on which aspect of the texture one wishes to show most clearly. For example, if the plastic deformation of a certain face-centered cubic material in sheet form were of concern, a (111) pole figure would be plotted because it would show at a glance the orientation of the {111} slip planes. Similarly, if the magnetic behavior of iron sheet is of interest, a (100) pole figure would be preferred, because the directions of high magnetic permeability in iron are ⟨100⟩ directions.

The pole figure of a fiber texture necessarily has rotational symmetry about the fiber axis (Fig. 14-10). The degree of scatter of this texture is given by the angular

[5] If the orientation is random, there will be equal numbers of poles in equal areas on the surface of a reference sphere centered on the specimen. There will not be equal numbers, however, on equal areas of the pole figure, since the stereographic projection is not area-true. This results, for randomly oriented grains, in an apparent clustering of poles at the center of the pole figure, since distances representing equal angles are much smaller in this central region than in other parts of the pole figure.

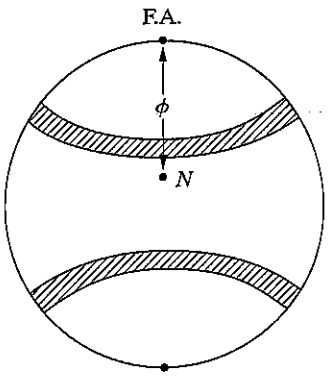

Figure 14-10 (111) pole figure for an imperfect [100] fiber texture. F.A. = fiber axis. Cross-hatched areas are areas of high (111) pole density.

width of the bands that show where (111) poles are located. The angle ϕ is the angle between the fiber axis and the general position N of any pole being considered. For the texture shown the bands are centered on ϕ values, measured from the top and bottom of the projection, of 54.7°, because this is the angle between the [100] fiber axis and the (111) poles being displayed.

Because of its rotational symmetry a pole figure of a fiber texture displays redundant information, in the sense that the pole density along any longitude line (meridian) is the same as along any other. Thus a plot of pole density vs. angle ϕ between 0 and 90^0 is a simpler description of the texture; for the texture shown in Fig. 14-10, such a plot would show a single maximum at 54.7°.

When the grain size of the specimen is small, as it normally is, separate determination of the orientations of a representative number of grains, as suggested by Fig. 14-9, is out of the question. Instead, x-ray methods are used in which the diffraction effects from thousands of grains are automatically averaged. The (*hkl*) pole figure of a fine-grained material is constructed by analyzing the distribution of intensity around the circumference of the corresponding *hkl* Debye ring. Two methods of doing this are available, the area detector[6] and the diffractometer method, and both are time consuming.

Although only a pole figure can provide a complete description of preferred orientation, some information can be obtained fairly quickly by a comparison of calculated diffraction line intensities with those observed on an ordinary diffractometer scan. As stated in Sec. 4-12, relative line intensities are given accurately by Eq. (4-21) only when the crystals of the specimen have completely random orientations. Therefore any radical disagreement between observed and calculated intensities is immediate evidence of preferred orientation in the specimen, and, from the nature of the disagreement, certain limited conclusions can usually be drawn con-

[6] The term "area detector" has been substituted here for the earlier designation of "photographic." Before the development of modern x-ray detectors, photographic emulsions were the only such detectors. Now image plates, CCD detectors or multiwire detectors would be used in place of film, and the more inclusive "area detector" seems more appropriate.

cerning the nature of the texture. For example, if a sheet specimen is examined in the diffractometer in the usual way (the specimen making equal angles with the incident and diffracted beams the parafocusing geometry), then the only grains which can contribute to the *hkl* reflection are those whose (*hkl*) planes are *parallel to the sheet surface*. If the texture is such that there are very few such grains, the intensity of the *hkl* reflection will be abnormally low. In another case, a given reflection may have abnormally high intensity, which would indicate that the corresponding planes were preferentially oriented parallel or nearly parallel to the sheet surface. As an illustration, the 200 diffractometer reflection from a specimen having the cube texture is abnormally high, and from this fact alone it is possible to conclude that there is a preferred orientation of (100) planes parallel to the sheet surface. The bottom diffractometer scan of Fig. 14-2 shows a platinum sheet with cube texture. However, no conclusion is possible as to whether or not there is a preferred direction in the (100) plane parallel to some reference direction on the sheet surface. Such information can be obtained only by making a pole figure.

14-8 THE TEXTURE OF WIRE (AREA DETECTOR METHOD)

The chief problem presented by a fiber texture is the identification of the fiber axis [*uvw*]. This can be done fairly easily with a single two-dimensional pinhole diffraction pattern, and the procedure is described in this section. If, in addition, the amount of scatter in the texture must be determined, a diffractometer method is preferable (Sec. 14-10) although image plates appear to provide a convenient alternative [14.13, 14.14].

The wire is examined in a transmission pinhole camera with filtered or crystal-monochromatized radiation and with the wire axis vertical, parallel to one edge of the flat area detector. The problem of finding the indices [*uvw*] of the fiber axis is best approached by considering the diffraction effects associated with an ideal case, for example, that of a wire of a cubic material having a perfect [100] fiber texture. Consider the 111 reflection. In Fig. 14-11, the wire specimen is at *C* with its axis along *NS*, normal to the incident beam *IC*. *CP* is the normal to a set of (111) planes. Diffraction from (111) can occur only when they are inclined to the incident beam at an angle θ which satisfies Bragg's law, and this requires that the (111) pole lie somewhere on the circle *PUQV*, since then the angle *PCI* between the plane normal and the incident beam will always be 90°–0. For this reason, *PUQV* is called the *reflection circle*. If the grains of the wire had completely random orientations, then (111) poles would lie at all positions on the sphere surface and therefore at all positions on the reflection circle, and the 111 reflection would consist of the complete Debye ring indicated in the drawing. But if the wire has a perfect [100] fiber texture, then the diffraction pattern produced by a stationary specimen is identical with that obtained from a single crystal rotated about the axis [100], because of the rotational symmetry of the wire. During this rotation, the (111) pole is confined to the small circle *PAQB*, all points of which make a constant angle $\phi = 54.7°$ with the [100] direction *N*. Therefore, the only (111) planes in the specimen that are able to

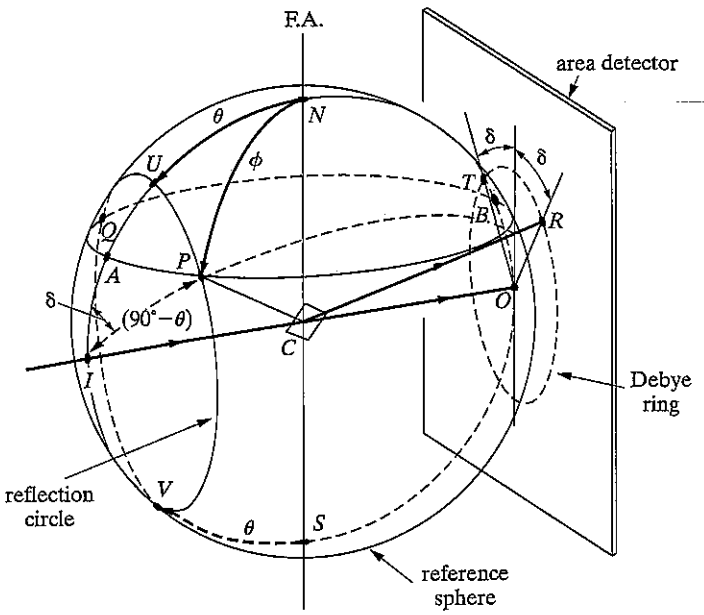

Figure 14-11 Geometry of diffraction from material having a fiber texture. F.A. = fiber axis.

diffract are those with poles at the intersections of the reflection circle and the circle *PAQB*. These intersections are located at *P* and *Q*, and the corresponding diffraction spots at *R* and *T*, at an azimuthal angle δ from a vertical line through the center of the film. Two other spots, not shown, are located in symmetrical positions on the lower half of the film. If the texture is not perfect, each of these spots will broaden peripherally into an arc whose length is a function of the degree of scatter in the texture.

By solving the spherical triangle *IPN*, results the following general relation results between the angles ϕ, θ, and δ:

$$\cos \phi = \cos \theta \cos \delta \tag{14-8}$$

These angles are shown stereographically in Fig. 14-12, projected on a plane normal to the incident beam. The (111) pole figure in (a) consists simply of two arcs which are the paths traced out by {111} poles during rotation of a single crystal about [100]. In (b), this pole figure has been superimposed on a projection of the reflection circle in order to find the locations of the diffraction plane normals. Radii drawn through these points (*P*, *Q*, *P'*, and *Q'*) then enable the angle δ to be measured and the appearance of the diffraction pattern to be predicted.

An unknown fiber axis is identified by measuring the angle δ on the film or area detector and obtaining ϕ from Eq. (14-8). When this is done for a number of different *hkl* reflections, a set of ϕ values is obtained from which the indices [*uvw*] of

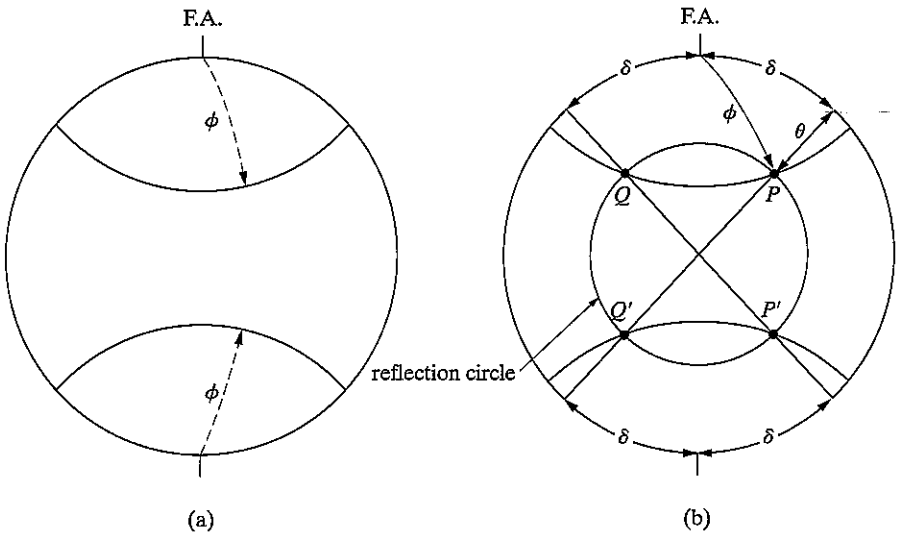

Figure 14-12 Perfect [100] fiber texture (a) (111) pole figure; (b) location of reflecting plane normals.

the fiber axis can be determined. The procedure will be illustrated with reference to the diffraction pattern of drawn aluminum wire shown in Fig. 14-13, which has the incomplete Debye rings typical of a pronounced texture. The first step is to index the Debye rings. Values of θ for each ring are calculated from measurements of ring diameter, and *hkl* indices are assigned by the use of Eq. (3-11) and Appendix 9. In this way the inner ring is identified as a 111 reflection and the outer one as 200. The angle δ is then measured from a vertical line through the center of the film to the center of each strong Debye arc. The average values of these angles are given below, together with the calculated values of ϕ:

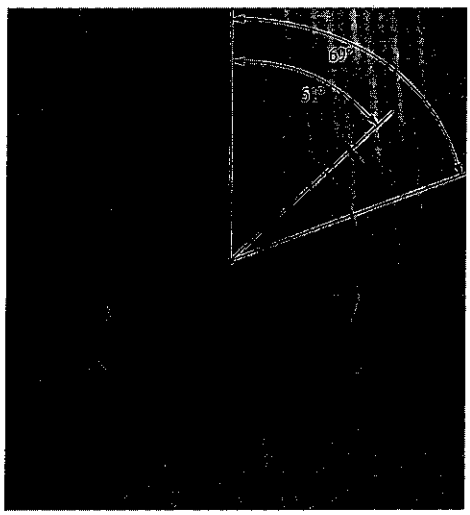

Figure 14-13 Transmission pinhole pattern of cold-drawn aluminum wire, wire axis vertical. Filtered copper radiation. (The radial streaks near the center are formed by the white radiation in the incident beam.)

Line	*hkl*	$\delta°$	$\theta°$	$\phi°$
Inner	111	69	19.3	70
Outer	200	52	22.3	55

The normals to the (111) and (200) planes therefore make angles of 70° and 55°, respectively, with the fiber axis. The indices [*uvw*] of this axis are determined either by the graphical construction shown in Fig. 16-8 or by inspection of a table of interplanar angles. In this case, inspection of Table 2-4 shows that [*uvw*] must be [111], since the angle between ⟨111⟩ and ⟨111⟩ is 70.5 and that between ⟨111⟩ and ⟨100⟩ is 54.7°, and these values agree with the values of ϕ given above within experimental error. The fiber axis of drawn aluminum wire is therefore [111]. There is some scatter of the [111] direction about the wire axis, however, inasmuch as the reflections on the film are short arcs rather than sharp spots. This can be taken into account by measuring the angular range of δ for each arc and calculating the corresponding range of ϕ. A (111) pole figure of the wire would then resemble Fig. 14-10.

Close inspection of Fig. 14-13 reveals a weak maximum on the outer ring (200 reflection) at the equator ($\delta = 90°$), indicating a weak [100] component in the texture; there is also evidence of this component on the inner 111 ring. This wire therefore has a double fiber texture: [111] strong and [100] weak. The relative amounts of these components can be measured from the output of as area detector or with a diffractometer (Sec. 14-10).

If a coating, such as an electrodeposit, on a flat sheet has a fiber texture with the fiber axis [*uvw*] normal to the sheet, then the (*hkl*) planes normal to [*uvw*] will be parallel, or nearly parallel, to the sheet surface. Unusual diffraction effects can then occur:

1. *Parafocusing diffractometer.* The incident and diffracted beams make the same angle with the sheet surface, so that the *hkl* reflection is abnormally strong and all others weak or absent.
2. *Back-reflection pinhole camera.* If the incident beam is normal to the sheet specimen and therefore parallel to the fiber axis, and a projection like that shown in Fig. 14-12(b) is made (projection plane parallel to sheet), then both the incident beam and the fiber axis coincide with the center of the projection. If the texture is ideally sharp, the (*hkl*) pole figure will consist of one or more concentric circles centered on the center of the projection, and the chance that one of these pole circles will coincide with the concentric reflection circle is essentially zero; no reflection will occur. But if the texture has enough scatter, one of the pole circles will broaden into a band wide enough to touch the reflection circle at all points; a Debye ring of *uniform* intensity will be formed. See Prob. 4-7. Thus a uniform Debye ring is not always evidence for randomly oriented grains.

14-9 THE TEXTURE OF SHEET (DIFFRACTOMETER METHODS)

Prior to about 1950, the texture of sheet materials was determined by a photographic method, in which diffracted x-ray intensities were visually estimated from the degree of film blackening on a series of photographs. The resulting pole figures were qualitative; they were divided by contour lines into areas in which the pole density was designated by terms such as low, medium, and high.

Once the photographic method was regarded as obsolete, because the diffractometer permited direct measurement of diffracted intensities and yielded quantitative pole figures. With the advent of the new area detectors, however, this method many regain its importance.

The essential difference between the area detectors and diffractometer methods can be understood by comparing Figs. 14-13 and 14-14. To analyze the information given in Fig. 14-13, the degree of film blackening, is estimated at points around the Debye ring. With a diffractometer (Fig. 14-14) the same nonuniform Debye ring exists in space, but the detector cannot be moved around the ring to explore the variation in intensity. Instead, the detector is fixed and *the specimen* is rotated. If the sheet specimen is rotated in its own plane, for example, the Debye ring rotates with it, and the high- and low-intensity regions are successively brought into a position where they can be measured by the detector. At each specimen position the intensity of the diffracted beam is taken to be proportional to the volume of grains then oriented to diffract that beam, except for corrections that may be necessary; this volume is in turn proportional to pole density.

To determine an (*hkl*) pole figure, the detector is fixed at the proper 2θ angle to receive the *hkl* reflection and the sheet specimen is rotated in particular ways described below. The pole figure is a projection made on a plane parallel to the sheet surface and therefore rotates with the sheet. But, whatever the orientation of the sheet, the normal N to the diffraction planes (*hkl*) remains fixed in space, bisecting the angle between the incident and diffracted beams. Therefore N can be imagined as moving over a fixed projection plane. The position of N on the pole figure

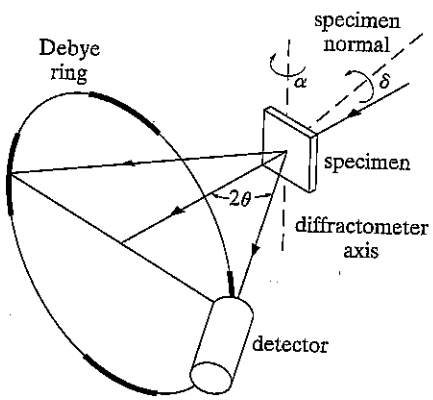

Figure 14-14 Transmission method for pole-figure determination. After Geisler [14.15].

is derived from the specimen rotation performed and at each position of N the pole density derived from the detector measurement of x-ray intensity can be plotted.

The ideal diffractometer specimen would be a small sphere cut out of the sheet, because a sphere presents the same aspect to the incident beam whatever its orientation. Normally, however, the sheet is examined directly, and then the paths of incident and diffracted beams within the sheet change with sheet orientation. It is then necessary to correct the measured intensities for these geometrical effects or to design the x-ray optics so that corrections are not required.

There is not one, but several, diffractometer methods for measuring sheet texture. They fall into two groups, transmission and reflection, both being normally necessary for complete coverage of the pole figure.

Transmission Methods

The two methods described below both require a specimen for which μt is of the order of 1, where μ is the linear absorption coefficient and t the thickness. This means a thickness of the order of 35 μm for iron examined with Mo $K\alpha$ radiation or 75 μm for aluminum with Cu $K\alpha$. Thicker sheet has to be thinned by grinding and etching.

The method of *Decker, Asp, and Harker* [14.16] was the first application of the diffractometer to texture measurements. The sheet specimen, in a special holder, is positioned initially with the rolling direction vertical and coincident with the diffractometer axis,[7] and with the plane of the specimen bisecting the angle between incident and diffracted beams (Figs. 14-14 and 14-15). The specimen holder allows rotation of the sheet in its own plane and about the diffractometer axis.

Figure 14-15 shows how to plot the pole N of the diffraction plane *hkl*. The angle α measures the amount of rotation about the diffractometer axis, positive when clockwise; α is zero when the sheet bisects the angle between incident and diffracted beams. The angle δ measures the amount by which the sheet is rotated in its own plane and is zero when the transverse direction is horizontal. (Note that other writers often have different symbols and definitions for these angles.) The pole N of the diffraction plane coincides initially, when α and δ are both zero, with the left transverse direction. A rotation of the specimen by δ degrees in its own plane then moves the pole of *hkl* δ degrees around the circumference of the pole figure, and a rotation of α degrees about the diffractometer axis then moves it α degrees from the circumference along a radius. To explore the pole figure, it is convenient to make intensity readings at intervals of 5° or 10° of α for a fixed value of δ: the pole figure is thus mapped out along a series of radii.[8] By this procedure the entire pole figure can be determined except for a region at the center extending from about

[7] For simplicity, the method is described here only in terms of a vertical-axis diffractometer.

[8] The chart shown in skeleton form in Fig. 14-15(b) is useful for this purpose. It is called a polar stereographic net, because it shows the latitude lines (circles) and longitude lines (radii) of a ruled globe projected on a plane normal to the polar NS-axis. In the absence of such a net, the equator or central meridian of a Wulff net can be used to measure the angle α.

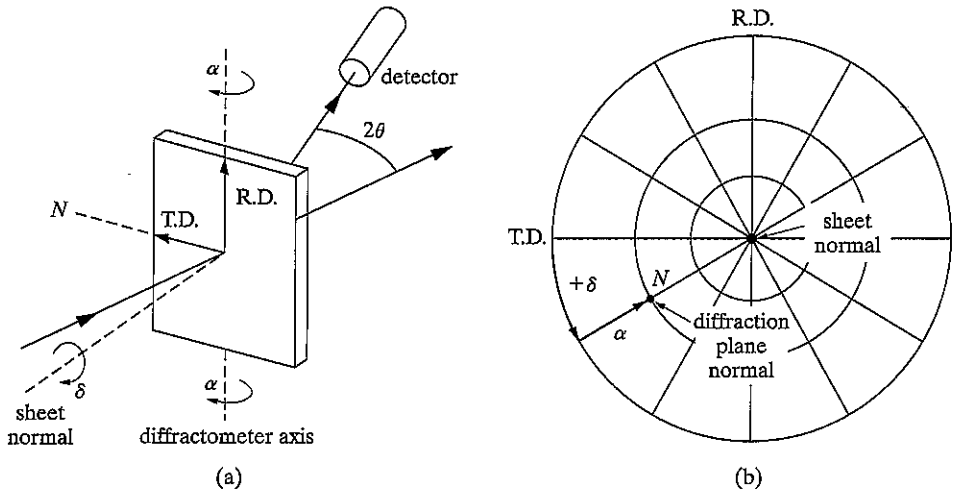

Figure 14-15 Angular relations in the transmission method, (a) in space, with $\alpha = \delta = \theta$ and (b) on the projection, with the diffraction plane normal N at $\alpha = \delta = 30°$. R.D. = rolling direction, T.D. = transverse direction.

$\alpha = 50°$ to $\alpha = 90°$; in this region not only does the absorption correction become inaccurate but the frame of the specimen holder obstructs the diffracted x-ray beam; the practical maximum value of α is thus reached before the theoretical, which is $90° - \theta$).

An absorption correction is necessary in this method because variations in α cause variations in both the volume of diffracting material and the path length of the x-rays within the specimen. Variations in δ have no effect. The angular dependence of the absorption factor is calculated by a method similar to that used for the reflection case considered in Sec. 4-10. The incident beam in Fig. 14-16 has intensity I_0 (ergs/cm^2/sec) and is 1 cm square in cross section. It is incident on a sheet specimen of thickness t and linear absorption coefficient μ, and the individual grains of this specimen are assumed to have a completely random orientation. Let a be the volume fraction of the specimen containing grains correctly oriented for diffraction of the incident beam, and b the fraction of the incident energy diffracted by a unit volume. Then the total energy per second in the diffracted beam outside the specimen, originating in a layer of thickness dx located at a depth x, is given by

$$dI_D = ab(DB)I_o e^{-\mu(AB+BC)}dx \text{ (ergs/see)}, \tag{14-9}$$

where

$$DB = \frac{1}{\cos(\theta - \alpha)}, \quad AB = \frac{x}{\cos(\theta - \alpha)}, \text{ and } BC = \frac{1 - x}{\cos(\theta + \alpha)}.$$

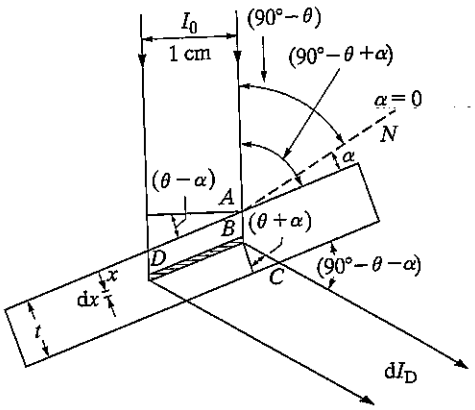

Figure 14-16 Path length and irradiated volume in the transmission method.

By substitution,

$$dI_D = \frac{abI_o}{\cos(\theta - \alpha)} e^{-\mu t/\cos(\theta+\alpha)} e^{-\mu x[1/\cos(\theta-\alpha) - 1/\cos(\theta+\alpha)]} dx. \qquad (14\text{-}10)$$

If $\alpha = 0$ is substituted into Eq. (14-10) and the integration from $x = 0$ to $x = t$ is performed, the total diffracted energy per second, the integrated intensity, for this position of the specimen is:[9]

$$I_D(\alpha = 0) = \frac{abtI_o}{\cos\theta} e^{-\mu t/\cos\theta}. \qquad (14\text{-}11)$$

When α is not zero, the same integration gives

$$I_D(\alpha = \alpha) = \frac{abI_o[e^{-\mu t/\cos(\theta-\alpha)} - e^{-\mu t/\cos(\theta+\alpha)}]}{\mu\{[\cos(\theta - \alpha)/\cos(\theta + \alpha)] - 1\}}. \qquad (14\text{-}12)$$

The ratio of these two integrated intensities is needed for the absorption correction and is:

$$R = \frac{I_D(\alpha = \alpha)}{I_D(\alpha = 0)} = \frac{\cos\theta\,[e^{-\mu t/\cos(\theta-\alpha)} - e^{-\mu t/\cos(\theta+\alpha)}]}{\mu t e^{-\mu t/\cos\theta}\{[\cos(\theta - \alpha)/\cos(\theta + \alpha)] - 1\}}. \qquad (14\text{-}13)$$

---

[9] In Sec. 7-9 mention was made of the fact that the diffracted beams in any transmission method were of maximum intensity when the thickness of the specimen was made equal to $1/\mu$. This result follows from Eq. (14-11). If $\theta = \alpha = 0$, then the primary beam will be incident on the specimen at right angles (sec Fig. 14-16), as in the usual transmission pinhole method, and the result will apply approximately to diffracted beams formed at small angles 2θ. The intensity of such a beam is given by

$$I_D = abtI_0e^{-\mu t}.$$

Differentiating this expression with respect to t and setting the result equal to zero shows that ID is a maximum when $t = 1/\mu$.

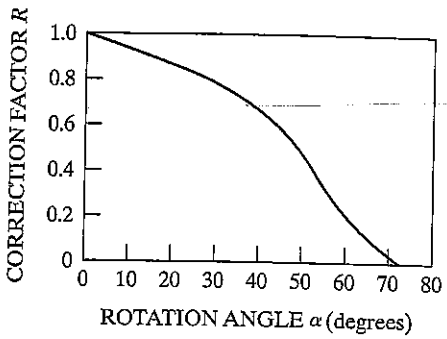

Figure 14-17 Variation of the correction factor R with α for clockwise rotation from the zero position. $\mu t = 1.0, \theta = 19.25°$.

A plot of R vs. α is given in Fig. 14-17 for typical values involved in the 111 reflection from aluminum with Cu $K\alpha$ radiation, namely, $\mu t = 1.0$ and $\theta = 19.25°$. Figure 14-17 shows that the integrated intensity of the reflection decreases as α increases in the clockwise direction from zero, even for a specimen containing randomly oriented grains. In the measurement of preferred orientation, it is therefore necessary to *divide* each measured intensity by the appropriate value of the correction factor R in order to arrive at a figure proportional to the pole density. From the way in which the correction factor R was derived, it follows that the *integrated intensity* of the diffracted beam must be measured. To do this with a fixed detector, the detector slits must be as wide as the diffracted beam for all values of α so that the whole width of the beam can enter the detector. The ideal incident beam for this method is a parallel one. However, a divergent beam may be used without too much error, provided the divergence is not too great. There is no question of focusing here: if the incident beam is divergent, the diffracted beam will diverge also and very wide detector slits will be required to admit its entire width. Clockwise rotation of the specimen about the diffractometer axis makes the diffracted beam narrower and is therefore preferred to counterclockwise rotation.

The value of μt used in Eq. (14-13) must be obtained by direct measurement, since it is not sufficiently accurate to use a tabulated value of μ together with the measured thickness t of the specimen. To determine μt use a strong diffracted beam from any convenient material and measure its intensity when the sheet specimen is inserted in the diffracted beam and again when it is not. The value of μt is then obtained from the absorption equation, $I_t = I_o e^{-\mu t}$, where I_o and I_t are the intensities incident on and transmitted by the sheet specimen, respectively.

The *Schulz transmission method* [14.17] uses a divergent, rather than a parallel, incident beam and a slit narrow enough to intercept only the central portion of the diffracted beam. For these conditions Schulz derived an equation, analogous to Eq. (14-12), relating the intensity diffracted by a random specimen (for brevity "random specimen" will be written for "specimen with randomly oriented grains") to the angular setting α. He also showed that the intensity diffracted by a random specimen was constant within a few percent up to an α value of about 30° for a sufficiently thin specimen ($\mu t = 0.4$ to 0.7) and small values of θ (less than about 20°); under these conditions the correction equation is not needed.

In tests of the correction equations by means of random specimens, Newkirk and Bruce [14.18] found good agreement with Eq. (14-13) of Decker, Asp, and Harker. On the other hand, the data of Aoki *et al.* [14.19] show better agreement between experiment and theory for the Schulz method than that of Decker *et al.* However, in judging the validity of correction equations one must always keep in mind the necessity not only of a truly random specimen, but also of a close match between the actual x-ray optics (nature of incident beam and width of detector slit) and those assumed in the derivation of the equations.

Reflection Methods

The central region of the pole figure is inaccessible to any transmission method and can be explored only by a reflection technique. The specimen must be of effectively infinite thickness or extra corrections will be required.

The most popular is the *Schulz reflection method* [14.20]. It requires a special specimen holder which allows rotation of the specimen in its own plane about an axis normal to its surface and about a horizontal axis; these axes are shown as BB' and AA' in Fig. 14-18. The horizontal axis AA' lies in the specimen surface and is initially adjusted, by rotation about the diffractometer axis, to make equal angles with the incident and diffracted beams. After this is done, no further rotation about the diffractometer axis is made. Since the axis AA' remains in a fixed position during the other rotations of the specimen, the irradiated surface of the specimen is always tangent to a focusing circle passing through the x-ray source and detector slit. A divergent beam may therefore be used since the diffracted beam will converge to a focus at the detector.

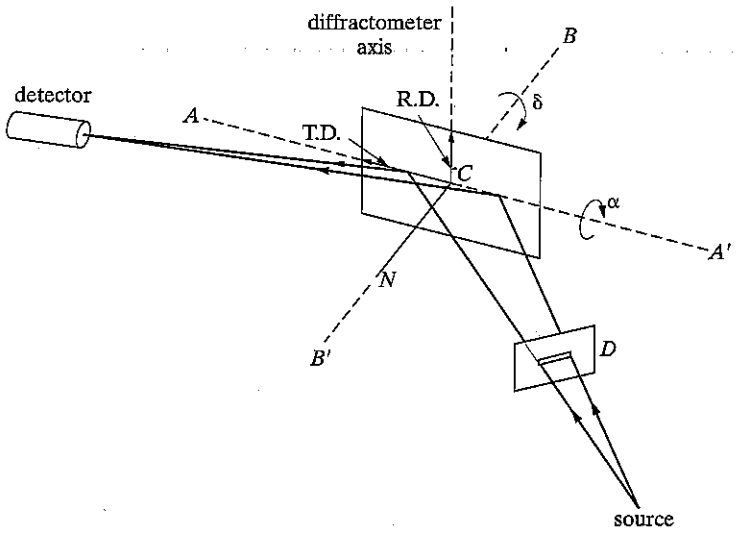

Figure 14-18 Schulz reflection method.

When the specimen is rotated about the axis AA', the axis BB' normal to the specimen surface rotates in a vertical plane, but CN, the diffraction plane normal remains fixed in a horizontal position normal to AA'. The rotation angles χ and ϕ are shown in Fig. 14-18.[10] The angle χ is zero when the sheet is horizontal and has a value of 90° when the sheet is in the vertical position shown in the drawing. In this position of the specimen, the diffraction plane normal is at the center of the projection. The angle ϕ measures the amount by which the rolling direction is rotated away from the left end of the axis AA' and has a value of +90° for the position illustrated. With these conventions the angles χ and ϕ may be plotted on the pole figure in the same way as α and δ in the transmission method [Fig. 14-15(b)].

The great virtue of the Schulz method is that no absorption correction is required for values of χ between 90° and about 40°, i.e., up to about 50° from the center of the pole figure. In other words, a random specimen can be rotated over this range of χ values without any change in the measured intensity of the diffracted beam, provided the specimen has effectively infinite thickness. Under these circumstances, the intensity of the diffracted beam is directly proportional to the pole density in the specimen, without any correction. The constancy of the absorption factor is due essentially to the narrow horizontal slit placed in the primary beam at D (Fig. 14-18), close to the specimen. The vertical opening in this slit is only about 0.5 mm, which means that the specimen is irradiated only over a long narrow rectangle centered on the fixed axis AA'. It can be shown [14.20] that a change in absorption does occur, as the specimen is rotated about AA', but it is exactly canceled by a change in the volume of diffracting material, the net result being a constant diffracted intensity for a random specimen when χ lies between 90° and about 40°. To achieve this condition, the reflecting surface of the specimen must be adjusted to accurately coincide with the axis AA' for all values of χ and ϕ. This adjustment is extremely important.

When the specimen is rotated out of the vertical position ($\chi < 90°$) in the sense shown in Fig. 14-18, the top part moves behind, and the bottom in front of, the focusing circle. The diffracted beam therefore widens at the detector slit and the measured diffracted intensity from a random specimen may decrease as χ departs from 90°. This effect is called the *defocusing error*. It may be minimized by slit adjustment (widening the detector slit and decreasing the vertical opening in slit D) or corrected by calculation [14.21, 14.22].

Figure 14-19 shows a specimen holder suitable for either transmission method and for the Schulz reflection method.

The *Field and Merchant reflection method* [14.23] is designed for a parallel incident beam, shown simply as a single line in Fig. 14-20. The specimen is placed initially with the rolling direction vertical, coincident with the diffractometer axis, the transverse direction horizontal, and the plane of the sheet equally inclined to the

[10] Designating the rotation angles as χ and ϕ distinguishes the reflection method from the transmission method where the angles are devoted α and δ, respectively.

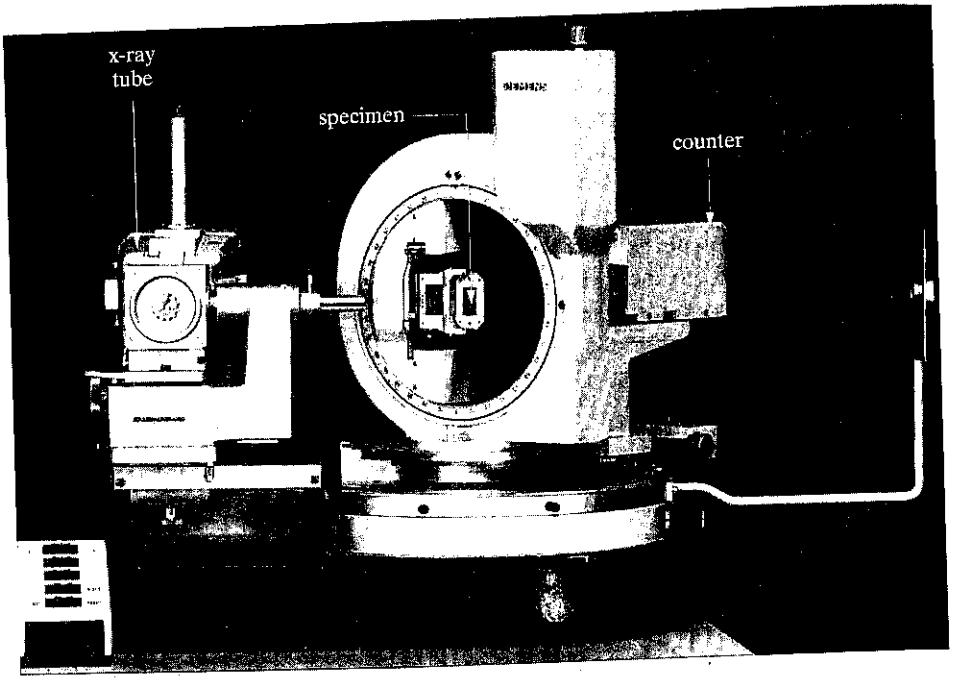

Figure 14-19 Pole-figure goniometer. The specimen shown is positioned for measurements by the transmission method, and a simple change in the orientation of the specimen holder allows measurements by the Schulz reflection method. The x-ray tube is seen here end-on. This instrument is designed for automatic operation. (Courtesy of Siemens Corporation.)

incident and diffracted beams; the pole N of the diffraction planes is then at the center of the projection ($\alpha = 90°$). Counterclockwise rotation of the specimen about the diffractometer axis, which incidentally will narrow the diffracted beam, moves N to the left along the equator ($\delta = 0$) of the pole figure. The angle δ is changed by rotating the specimen in its own plane.

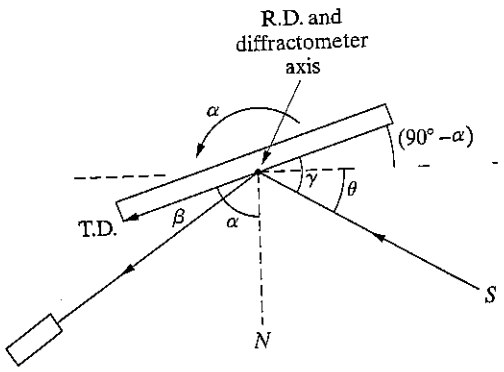

Figure 14-20 Field and Merchant reflection method. N = diffracting plane normal.

Diffracted intensities must be corrected for change in absorption due to change in α. The angles γ and β of incidence and reflection are the same as shown in Fig. 14-20, and Eq. (4-14) applies:

$$dI_D = \frac{I_o ab}{\sin \gamma} e^{-\mu x(1/\sin\gamma + 1/\sin\beta)} dx. \tag{4-14}$$

For counterclockwise rotation $\gamma = \theta + (90^o - \alpha)$ and $\beta = \alpha - (90^o - \theta)$. Making these substitutions into Eq. (4-14) and integrating from x = 0 to ∞, yields the integrated intensity:

$$I_D = \frac{I_O ab}{\mu\{1 - [\cos(\alpha - \theta)/\cos(\alpha + \theta)]\}}. \tag{14-14}$$

Only the ratio of this quantity to the same quantity for $\alpha = 90^o$ is of interest and it is

$$S = \frac{I_D(\alpha = \alpha)}{I_D(\alpha = 90°)} = 1 - \cot\alpha \cot\theta. \tag{14-15}$$

Diffracted intensities must be divided by S, which is independent of μ, to give values proportional to pole density. The correction is less severe (S closer to 1), the larger the value of θ; it is therefore advantageous to measure a higher order of the *hkl* reflection measured in transmission. The specimen holder can be identical with that used in the transmission method.

Plotting the Pole Figure

A transmission method yields pole densities covering the outer part of the pole figure, from $\alpha = 0$ to about 50°. A reflection method covers the inner part, from $\alpha =$ about 40° to 90° (i.e., $\chi =$ 90° to 40° in the Schulz method). The pole densities are in arbitrary units, either directly measured diffracted intensities or corrected intensities, depending on the method used. Along those radii of the pole figure where substantial pole density exists in the region of overlap of the two methods ($\alpha =$ 40° to 50°), a normalizing factor is found which will make the pole densities from the transmission method agree with those from the reflection method. The match in the overlap region is rarely perfect, but a substantial disagreement between normalizing factors for different radii points to experimental or computational errors.

Once one set of data is normalized to match the other set contour lines can be constructed on the pole figure at selected levels to connect points of the same pole density, and the result is a pole figure such as Fig. 14-21. Normally this is done using computer programs such as popLA [14.25]. Vendor-supplied software or custom written routines. Many, but not all, textures are symmetrical with respect to reflection planes normal to the rolling and transverse directions, and many published pole figures have been determined from measurements made only in one quadrant, with the other quadrants found by assuming symmetry, without supporting data.

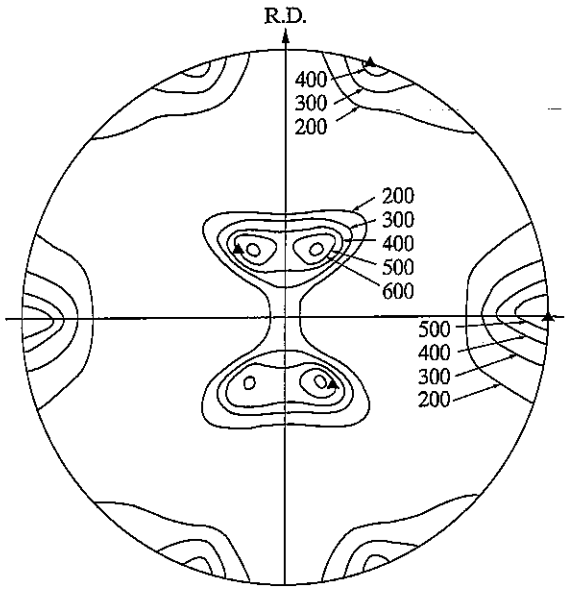

Figure 14-21 (111) pole figure of alpha brass sheet (70 Cu-30 Zn), cold rolled to a reduction in thickness of 95 percent. Pole densities in arbitrary units. The outer parts of all four quadrants were determined experimentally; the inner parts of the upper right and lower left quadrants were measured, and the other two constructed by reflection. The solid triangles show the (110) [112] orientation. Hu, Sperry, and Beck [14.24].

The deformation texture of brass sheet (Fig. 14-21) is fairly sharp, and it is then of interest to know whether or not it can be approximated by an "ideal orientation." To find this orientation successively lay several standard projections over the pole figure, looking for a match between (111) poles and high-density regions. The solid triangles in Fig. 14-21 show such a match: they represent the (111) poles of a single crystal oriented so that its (110) plane is parallel to the sheet and the [112] direction parallel to the rolling direction. Reflection of these poles in the symmetry planes of the texture, which is equivalent to adding orientations like $(110)[1\bar{1}2]$, will approximately account for all the high-density regions of the pole figure. This texture can therefore be represented by the ideal orientation $\{110\}\langle\bar{1}12\rangle$. It should be emphasized that the pole figure itself is a far better description of the texture than any bare statement of an ideal orientation, which says nothing about the scatter. A quantitative pole figure has about the same relation to an ideal orientation as an accurate contour map of a hill has to a statement of the height, width, and length of the hill.

Pole densities in arbitrary units are not as informative as those expressed in multiples of the pole density of a random specimen, so called "times random" units. The contour lines in Fig. 14-22 are marked with these units, and one can see at a glance those regions of the pole figure that have a higher, or lower, pole density than random; this pole figure, incidentally, was measured in all four quadrants. The texture represented there, of considerable industrial interest, is messy and cannot be well characterized by ideal orientations. It is approximately a $\langle 111\rangle$ fiber texture, with the fiber axis normal to the plane of the sheet, containing $\{111\}\langle 110\rangle$, called the "cube-on-corner" texture, as its strongest single component [14.26, 14.27].

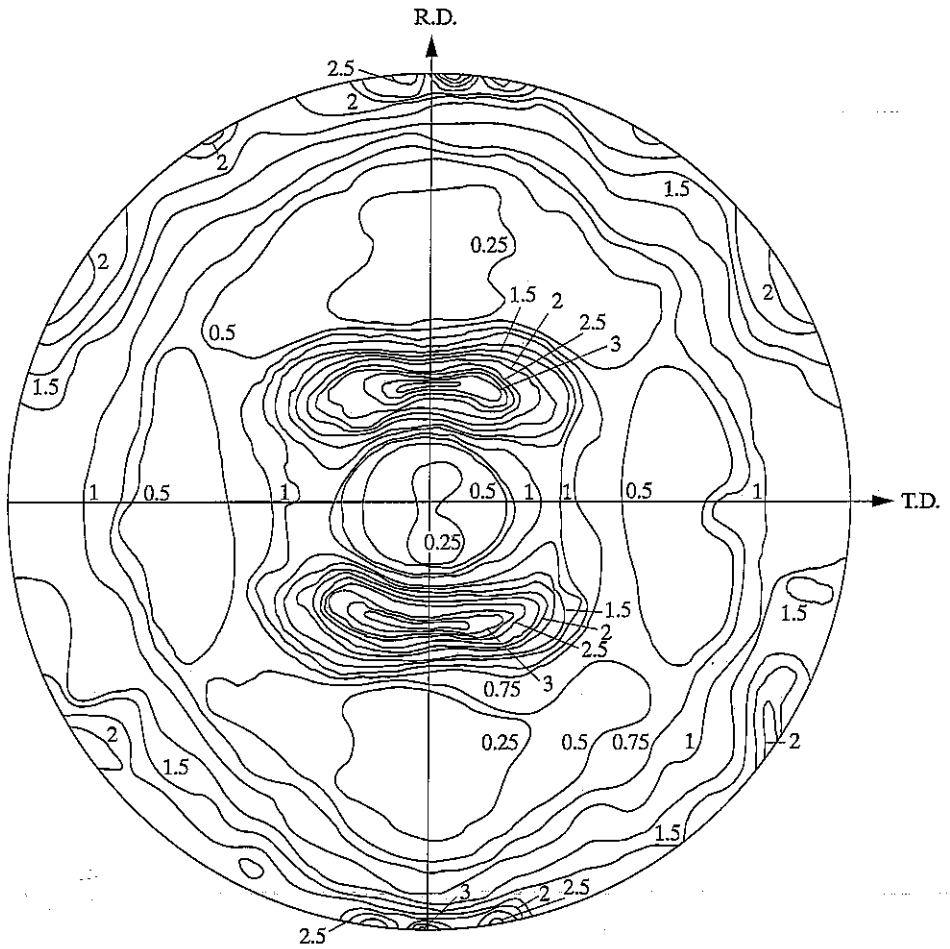

Figure 14-22 (110) pole figure of recrystallized commercial low-carbon (0.04 percent) sheet steel, aluminum killed, 0.9 mm thick. Pole densities in "times random" units. Determined by a reflection method from composite specimens; see text under "General." Bunge and Roberts [14.26].

Diffracted intensities, proportional to pole densities, may be put on a times-random basis by comparing them with intensities diffracted by a random specimen [14-28]. The random specimen should be of the same material as the textured specimen and, for a transmission method, it should have the same value of μt; if not, a correction has to be made that will depend on the transmission method involved. The random specimen itself is usually made by compressing and sintering a power [14.18, 14.19]. The randomness of grain orientation in this specimen must be checked by determining its diffraction pattern with a diffractometer in the usual way; the measured integrated intensities of all lines should agree with those calculated by Eq. (4-21).

General

The conditions for optimum specimen thickness in transmission and infinite thickness in reflection are such that the same specimen can serve for both methods. The penalty for exceeding the optimum thickness is not severe: a thickness of double the optimum value for transmission at $\alpha = 0$ reduces the diffracted intensity by only 26 percent (Problem 14-8).

It may be difficult to make a thin specimen, particularly of a heavy metal, which has the required low, and *uniform*, value of μt throughout. Some investigators have therefore avoided a transmission method altogether by determining only the central portion of the pole figure by reflection; such partial pole figures are useful for some purposes. Others have obtained a complete pole figure by reflecting x-rays from a surface or surfaces inclined to the sheet surface. Several pieces of the sheet are stacked with rolling directions parallel and a composite specimen made by clamping or cementing the stack. If this specimen is cut to expose a surface whose normal makes the same angle, of 54.7°, with the sheet normal and rolling and transverse directions, then measurements on this surface by a reflection method will cover one quadrant of the pole figure [14.29]. The pole figure of Fig. 14-22 was derived from reflection measurements on the sheet plane and on sections normal to the rolling and transverse directions.

Errors that can affect texture measurements include the following:

1. If the grain size is too large, as in some recrystallized specimens, the incident beam will not sample enough grains for good statistical accuracy. The specimen holder should then include a mechanical device that will translate the specimen back and forth in its own plane in order to expose more grains to the incident beam.
2. The texture at the surface of a sheet can differ from that in the midplane [14.24]. When such a texture gradient exists, it must be remembered that the transmission and reflection methods preferentially sample different layers of the same specimen and that the thicknesses of the layers so sampled vary with α in a systematic way.
3. The x-ray optics, particularly slit sizes, must conform to those required by the x-ray method involved. Too narrow a detector slit will exclude a wanted part of the diffraction line; too wide a slit will include some of the background. Too often the background is simply ignored, with the result that measured intensities include both line and background; it would be highly beneficial to eliminate or reduce the background by means of a crystal monochromator, balanced filters, or a pulse-height analyzer. Errors from these sources can be large. They can be almost entirely eliminated by comparing intensities from the textured specimen with intensities measured under identical conditions from a truly random specimen, provided the two specimens differ only in grain orientation. Such a random specimen can be very hard to make. (Note, for example, that an annealed random specimen

will have narrower diffraction lines than a cold-worked textured specimen.)

Because the manual determination of preferred orientation is rather tedious, the process has been automated, and a variety of instruments are available from vendors (Fig. 14-19). Under computer control, the angular settings α and δ (or χ and ϕ) of the specimen are varied in a prescribed sequence by motor drive, and the diffracted intensity at each setting is recorded, on disk.

The *analysis* of preferred orientation has now gone beyond pole figures, in the direction of a more complete description of the texture. Establishing experimentally that a certain crystal in a sheet has a (100) pole, for example, located at a point on the pole figure specified by the angles α and δ, does not fully specify the orientation of the crystal. These two angles merely describe the orientation of the direction [100], and the crystal might have any rotational position about this axis. A third angle is needed to fix the orientation of the crystal. A full description of the texture would require the specification of three angles (called Ψ, θ, ϕ) for each crystal in the sheet. This information is contained in the *crystal orientation distribution function* or *odf* which is discussed in Sec. 14-11.

14-10 THE TEXTURE OF WIRE (DIFFRACTOMETER METHOD)

As mentioned in Sec. 14-7, if a wire or rod has a true fiber texture, its pole figure will have rotational symmetry about the fiber axis and will resemble Fig. 14-10 Therefore the pole density must be measured only along a single radius. The angle between the pole N and the fiber axis F.A. is usually called ϕ when dealing with fiber textures.

The Field and Merchant method may be used to measure pole density, and two specimens are required to cover the entire 90° range of ϕ:

1. *Low-ϕ region.* X-rays are diffracted from the cross section of the wire, as in Fig. 14-23(a). The specimen is a bundle of wires, packed together and cemented into a rectangular hole cut in a thick plastic disc; the wire ends are then ground, polished, and etched. This cross section is made initially parallel to the diffractometer axis and equally inclined to the incident and diffracted beams. The angle ϕ measures the counterclockwise rotation of the specimen about the diffractometer axis from this initial position. Next define a new angle ρ as the acute angle between the specimen surface and the diffraction-plane normal N. The angle α of Eq. (14-14) and Fig. 14-20 becomes $\rho = \rho_L = 90^o - \phi$, so that

$$W = \frac{I_D(\rho = \rho)}{I_D(\rho = 90°)} = 1 - \cot\rho \cot\theta. \tag{14-16}$$

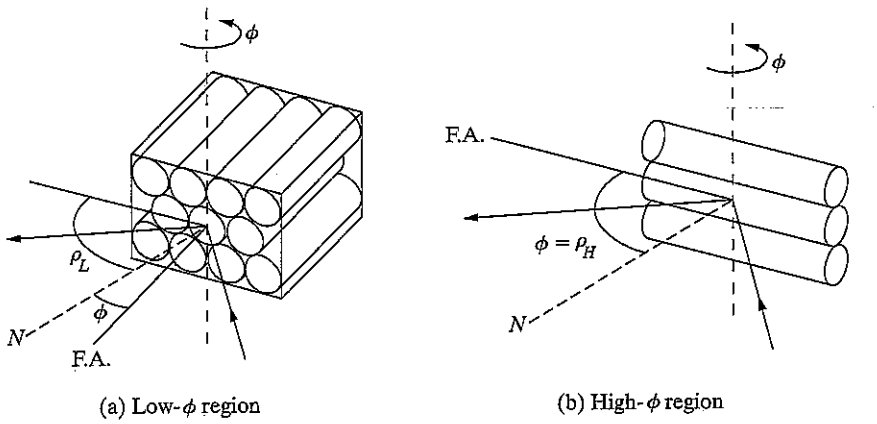

(a) Low-ϕ region (b) High-ϕ region

Figure 14-23 Diffraction from composite wire specimens. ϕ is angle between fiber axis F.A. and diffraction-plane normal N. ρ is angle between N and specimen surface.

Diffracted intensities are to be divided by W to obtain numbers proportional to pole density.

2. *High-ϕ region.* X-rays are diffracted from the side of the wire, as in Fig. 14-23 (b). The specimen is a set of wires glued to a grooved plate. Equation (14-16) still applies, but now $\alpha = \rho = \rho_H = \phi$.

When the diffracted intensities I_D given by each method have been divided by W and normalized in the region of overlap, a set of numbers I is obtained which is proportional to pole density. Figure 14-24 shows an I, ϕ curve obtained in this way for the inside texture of cold-drawn aluminum wire. The peaks at $\phi = 0$ and 70° are due to the strong [111] component of the texture and the peak at 55° to a weak [100] component.

By analysis of an I, ϕ pole density curve the pole densities can be put on a times-random basis and determine the relative amounts of the components in a double or multiple fiber texture can be determined [14.31-14.33].

Imagine a reference sphere of unit radius centered on the wire (Fig. 14-25). The element of area on the surface is $dA = 2\pi \sin\phi \, d\phi$. If I is the pole density, the number of (hkl) poles in this area is $dn = I \, dA = 2\pi I \sin \phi \, d\phi$, and the total number of poles on the surface of a hemisphere is

$$n = 2\pi \int_0^{\pi/2} I \sin \phi \, d\phi. \tag{14-17}$$

If I_r is the pole density of a random specimen, then $n = I_r(2\pi)$. Therefore

$$I_r = \int_0^{\pi/2} I \sin \phi \, d\phi. \tag{14-18}$$

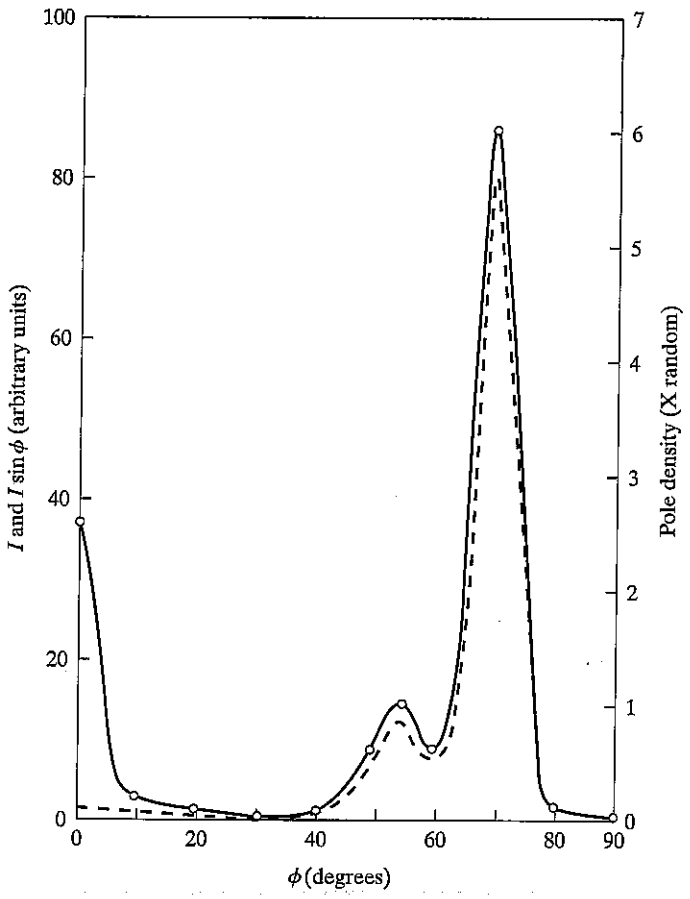

Figure 14-24 (111) pole density I (full curve) and $I \sin \phi$ (dashed) as a function of ϕ for a cold-drawn aluminum wire, reduced in area 95 percent by drawing, and etched to 80 percent of the as-drawn diameter. Final specimen diameter 1.3 mm, Cr Kα radiation, 222 reflection. Freda *et al.* [14.30].

This integral is simply the area under a curve of $I \sin \phi$ vs. ϕ, and this area in turn is equal to the average ordinate of the curve $\langle I \sin \phi \rangle_{av}$ times $\pi/2$. Therefore,

$$I_r = \frac{\pi}{2} \langle I \sin \phi \rangle_{av}. \tag{14-19}$$

This relation is valid whether the n poles are distributed randomly on the sphere or in some preferred manner, and it allows determination of I_r from measurements on a textured specimen. From experimental I, ϕ data construct a curve of $I \sin \phi$ vs. ϕ, shown dashed in Fig. 14-24, determine its average ordinate, and find I_r from Eq. 14-19. Once I_r is known (14.3 units for this wire), the I, sin ϕ pole density curve can be put on a times-random basis (right-hand ordinate). (Because the angular aperture of the detector slit is not small relative to ϕ when ϕ is small, the true pole

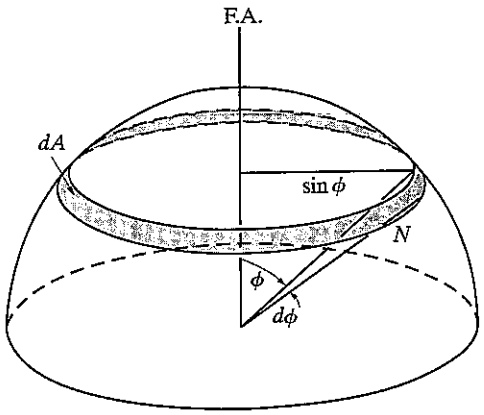

Figure 14-25 Element of area on reference sphere.

density I near $\phi = 0$ can only be approximated [14.32]. Therefore extrapolate the I sin ϕ curve near $\phi = 0$ rather than extend it to zero, as is mathematically indicated.)

The amount of each component in a double texture is proportional to the area under the peak(s) due to that component on a curve of I sin ϕ vs. ϕ; knowledge of the multiplicities involved can reduce the number of peaks that need be considered. The multiplicity of {111} poles is 8 for a sphere and 4 for a hemisphere. In Fig. 14-24 the [100] component puts four {111} poles per grain under the peak at 55°; the [111] component, on the other hand, has one {111} pole at 0° and three at 70°. Because of the uncertainty in the area of the peak at 0°, the area ascribed to the [111] component can be taken as 4/3 times the area of the peak at 70°. Therefore,

$$\frac{\text{Volume fraction of [111] component}}{\text{Volume fraction of [100] component}} = \frac{\left(\frac{4}{3}\right)(\text{area of } 70° \text{ peak})}{(\text{area of } 55° \text{ peak})}.$$

For the aluminum wire, this calculation led to volume fractions of 0.85 for the [111] component and 0.15 for the [100].

Note that this result was obtained without making any use of the measurements made at ϕ values less than 40°. Thus a complete pole density curve is not necessary for the evaluation of a texture, provided the texture is sharp enough to produce well resolved peaks in the high-ϕ region. This is a fortunate circumstance, because high-ϕ measurements require little or no specimen preparation.

Preferred orientation in wire does not always take the form of a pure fiber texture. For example, the deformation texture of iron wire is usually considered to be a [110] fiber texture, but Leber [14.34] showed that a *cylindrical texture* was also present. Such a texture may be regarded as a sheet texture, (100) [011] for iron, wrapped around the wire axis. Thus at any point on the wire surface, a (100) plane is tangent to the surface and a [011] direction parallel to the wire axis. The presence of a cylindrical component in a fiber texture is disclosed by anomalies in the I sin ϕ

curve: the areas under the peaks ascribed to the fiber-texture component will not be in the ratio to be expected from the multiplicities [14.35].

14-11 INVERSE POLE FIGURES

A pole figure shows the distribution of a selected crystallographic direction relative to certain directions in the specimen. Texture data may also be presented in the form of an *inverse pole figure*, which shows the distribution of a selected direction *in the specimen* relative to the crystal axes. The projection plane for an inverse pole figure is therefore a standard projection of the crystal, of which only the unit stereographic triangle need be shown. Both wire and sheet textures may be represented.

Figure 14-26(a) is an inverse pole figure for the inside texture of an extruded aluminum rod, showing the density distribution of the rod axis on a times-random basis. It was derived by a trial-and-error method [14.31] from pole density curves, as in Fig. 14-24, for the (001), (111), and (113) poles. Note the concentrations of the rod axis at [001] and [111], indicating a double fiber texture; the volume fractions of the [001] and [111] components were estimated as 0.53 and 0.47, respectively. Note that an inverse pole figure shows immediately the crystallographic "direction" of the scatter. In this double texture, there is a larger scatter of each component toward one another than toward [011].

Sheet textures require three separate inverse pole figures to show the distribution of the sheet normal, rolling direction, and transverse direction. Figure 14-26(b) is such a projection for the normal direction of the steel sheet whose (110) pole figure was given in Fig. 14-22; it was calculated from the orientation distribution function mentioned in Sec. 14-9. The distribution of the normal direction is also shown in (c), for the same material, but this distribution was measured directly in the following way. A powder pattern is made of the sheet in a diffractometer by the usual method, with the sheet equally inclined to the incident and diffracted beams i.e., in the normal parafocusing geometry. The intensity of any *hkl* reflection, relative to that from a random specimen, is then proportional to the volume fraction of grains having their (*hkl*) planes parallel to the sheet surface, or to the volume fraction of grains having the sheet normal parallel to the (*hkl*) normal. Stated another way, and with specific reference to Fig. 14-26(c), the probability of the sheet normal in this steel being parallel to [111] is 3.97 times normal. Similar data for the rolling direction, for example, are obtained by diffracting x-rays from a surface normal to the rolling direction, a surface exposed by sectioning a stack of sheets. This method produces only as many data points in the stereographic triangle as there are lines on the powder pattern and is therefore better suited to materials of low crystal symmetry than to cubic materials.

The inverse pole figures of Figs. 14-2.6(b) and (c) both show a high density of (111) poles parallel to the sheet normal and are therefore consistent with the [111] quasi-fiber texture mentioned in Sec. 14-9.

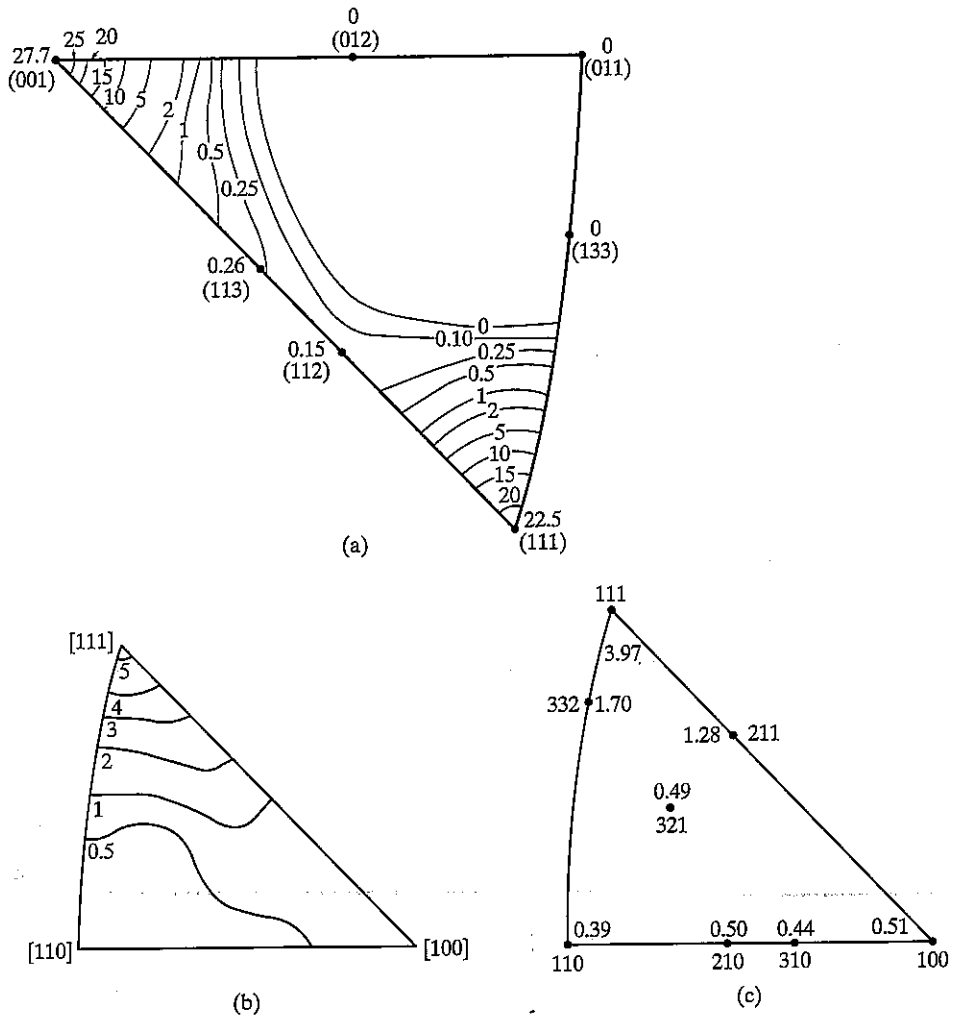

Figure 14-26 Inverse pole figures. (a) Distribution of axis of aluminum rod, extruded at 450°F to a reduction in area of 92 percent and a final diameter of 23 mm. Jetter, McHargue, and Williams [14.31]. (b) and (c) show the distribution of the sheet normal for the steel sheet of Fig. 14.22. Bunge and Roberts [14.26].

The inverse pole figure is the best way to represent a fiber texture, but it offers no advantage over a direct pole figure in the description of a sheet texture. Inverse or direct, a pole figure is a two-dimensional plot that fixes, at a point, only a direction in space, be it crystal space or specimen space. Only the three-dimensional "plot" afforded by the orientation distribution (see below) can completely describe the orientations present, and this approach, being quite general, is just as applicable to fiber textures as it is to sheet.

14-12 ORIENTATION DISTRIBUTION FUNCTIONS

In Sec. 14-9, three angles were seen to be needed to uniquely fix the orientation of a given crystal relative to the sample coordinate system (i.e., rolling direction, sheet normal, etc.). Methods of calculating this orientation distribution function from pole figures have been developed by Roe, Bunge, and Williams [14.36-14.39]. The mathematics involved are complex and the calculations extensive, but this approach is powerful and of great generality.

The orientation distribution function for a cubic material in sheet form can be calculated from any two experimental pole figures, for example, the (100) and (110). Once the distribution is known, any other desired pole figure can be calculated, for example, the (111); it need not be measured. It is even possible to calculate the orientation distribution from a set of partial pole figures, determined by a reflection method out of 60° from the center of the pole figure ($\gamma = 30°$) [14.40]. The orientation distribution function itself is usually presented in the form of crystal density plots, in which the density is shown as a contour map, for example, in angle space. One method uses spherical polar coordinates θ and ψ to specify the direction of the rotation axis relating the crystal axes to the sample coordinate system and rotation angle ω about the axis. Euler angles φ_1, φ_2 and Φ can also be used (Fig. 14-27). A series of constant φ_2 is typically used to present all of the information, and Fig. 14-28 gives an example for rolled brass [14.41].

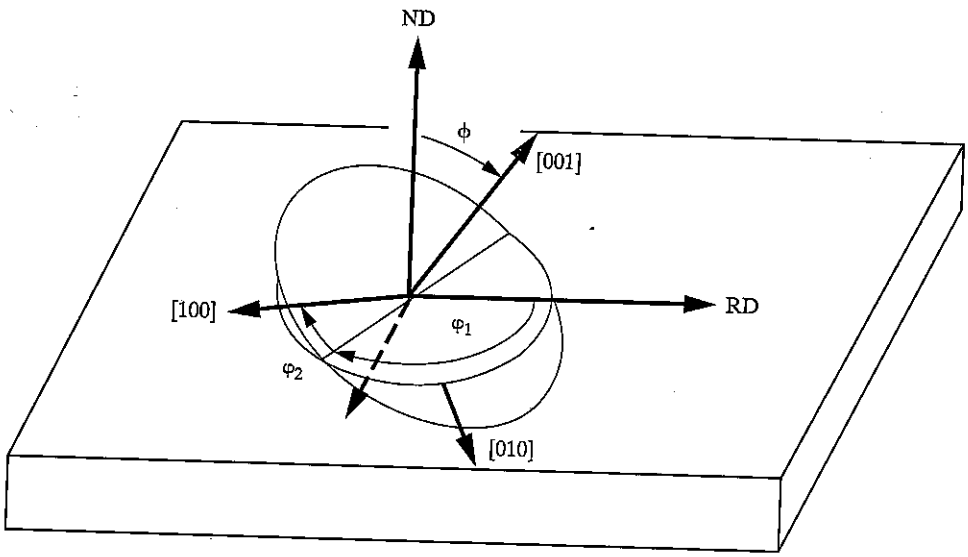

Figure 14-27 Definition of orientation of crystal axes in terms of Euler angles φ_1, ϕ and φ_2 defined relative to the sample reference directions, here the rolling direction RD and the normal direction ND. After [14.41].

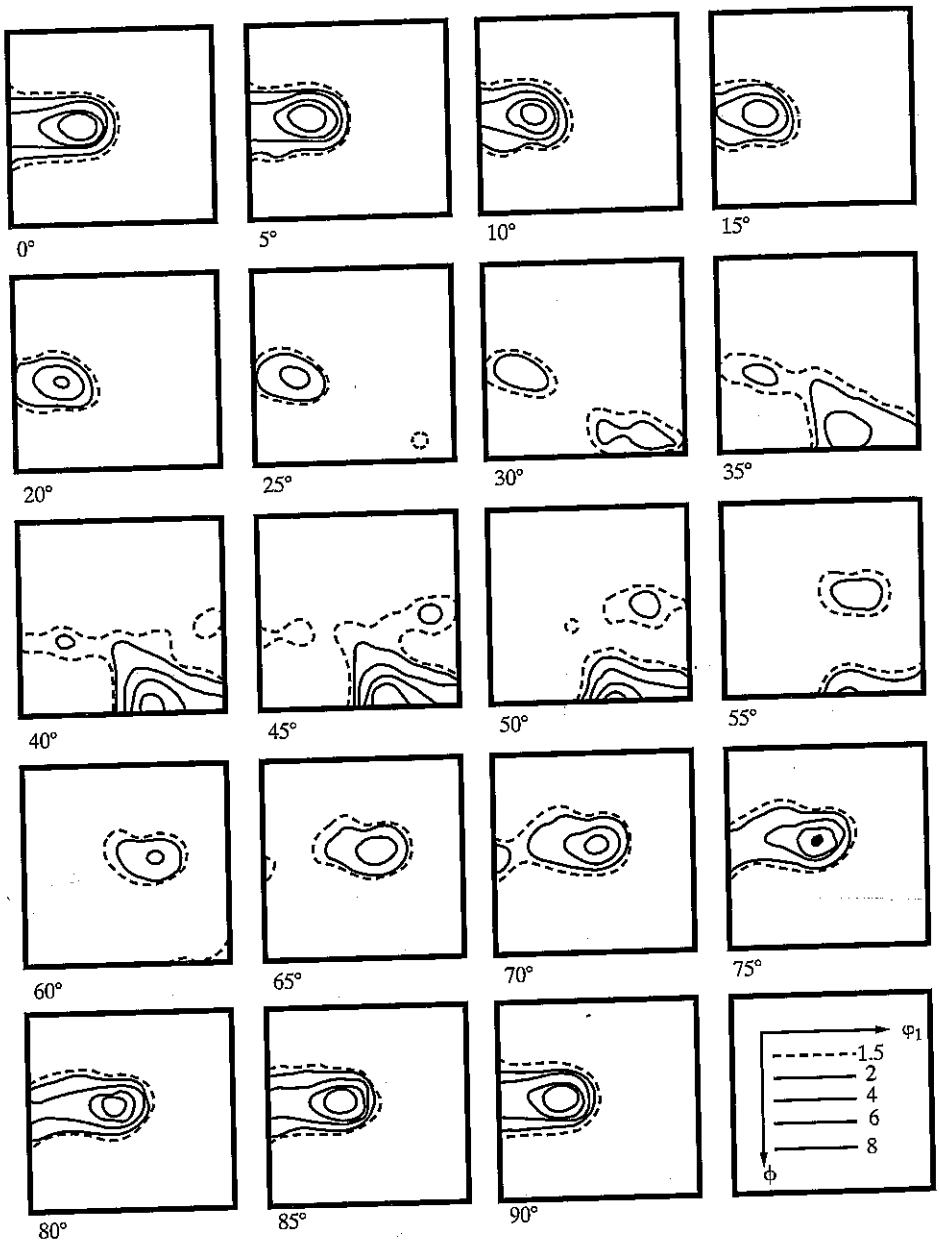

Figure 14-28 Orientation distribution function for brass cold-rolled 95%. Planes of constant φ_2 spaced every 5° are shown. The contours of equal density (times random) and orientations of φ_1 and ϕ are shown at the lower right. [14.41].

14-13 AMORPHOUS AND SEMI-AMORPHOUS SOLIDS

This chapter has concentrated on crystalline materials. X-ray diffraction can also furnish structural information about amorphous and semi-amorphous solids, even though the "structure" is much more diffuse.

Most glasses are amorphous. They yield a pinhole pattern consisting only of a broad, diffuse halo around the central spot, corresponding to the single maximum in the scattering curve of Fig. 5-10. Analysis of this curve yields such information as average interatomic distances and average number of atoms around a given atom. The theory of diffraction by amorphous substances is covered briefly in Chap. 18 and is treated in the books of Guinier [G. 30] and Warren [G. 20].

Many polymeric materials are partly crystalline: They are composed of very long molecules, generally in a state of great disarray but here and there organized into ordered regions usually called "crystallites." These regions, typically very small and highly strained, produce very broad diffraction lines. By comparing the integrated intensity of these lines with that of the broad halo due to the amorphous regions, the volume fraction of crystallites, called the "degree of crystallinity" of the polymer, can be estimated. X-ray diffraction can also disclose crystallite size, usually by means of the Scherrer equation for line broadening (Eq. 5-2), and preferred orientation. The latter condition is quite common in fibers and sheets and is studied by one or more of the methods described in this chapter. In fact, the alignment of crystallites in natural fibers like cotton and silk has long been known and is the origin of the term "fiber texture" to describe the preferred orientation found in metal wires. The particular applications of x-ray methods to the study of polymers is the subject of a book by Alexander [14.42].

14-14 SUMMARY

In this chapter various aspects of the structure of polycrystalline aggregates and the quantitative effects of variations in crystal size, quality, and orientation on the diffraction pattern have been examined. Although a complete investigation of the structure of an aggregate requires a considerable amount of time and rather complex apparatus, the very great utility of the simple pinhole photograph should not be overlooked. It is surprising how much information an experienced observer can obtain simply by inspection of a pinhole photograph, without making any measurements on the film and without any knowledge of the specimen, i.e., without knowing its chemical identity, crystal structure, or even whether it is amorphous or crystalline. The latter point can be settled at a glance, since Debye rings indicate crystallinity and broad haloes an amorphous condition. If the specimen is crystalline, the conclusions that can be drawn from the appearance of the lines are summarized in Table 14-3.

TABLE 14.3

Appearance of diffraction lines	Condition of specimen
Continuous	Fine-grained (or coarse-grained and cold-worked)
Spotty	Coarse-grained
Narrow (1)	Strain-free
Broad (1)	Residual stress and possibly small particle size (if specimen is a solid aggregate) Small particle size (if specimen is a brittle powder)
Uniform intensity	Random orientation (2)
Nonuniform intensity	Preferred orientation

(1) Best judged by noting whether or not the Kα doublet is resolved in back reflection.
(2) Or possibly presence of a fiber texture, if the incident beam is parallel to the fiber axis.

PROBLEMS

14-1 Prove the statement made in Sec. 4-10 that the effective irradiated volume of a flat plate specimen in a diffractometer is constant and independent of θ.
14-2 For given values of θ and μ, which results in a greater effective depth of x-ray penetration, a back-reflection pinhole camera or a diffractometer?
14-3 Assume that the effective depth of penetration of an x-ray beam is that thickness of material which contributes 99 percent of the total energy diffracted by an infinitely thick specimen. Calculate the penetration depth in μm for a low-carbon steel specimen under the following conditions:

a) Diffractometer; lowest-angle reflection; Cu $K\alpha$ radiation.
b) Diffractometer; highest-angle reflection; Cu $K\alpha$ radiation.
c) Diffractometer; highest-angle reflection; Cr $K\alpha$ radiation.
d) Back-reflection pinhole camera; highest-angle reflection; Cr $K\alpha$ radiation.

14-4 If the same hkl reflection from a given material is examined in a diffractometer with successively different wavelengths, how does the penetration depth x vary with λ? (Assume the wavelengths used lie on the same branch of the absorption curve of the material.)
14-5 (a)A transmission pinhole photograph is made of a sheet specimen of thickness t and linear absorption coefficient μ. Show that the fraction of the total diffracted energy in any one reflection contributed by a layer of thickness w is given by

$$T = \frac{e^{-\mu[x+(t-x)/\cos+2\theta]}\left[e^{-\mu w(1-1/\cos 2\theta)} - 1\right]}{e^{-\mu t} - e^{-\mu t/\cos 2\theta}},$$

where x is the distance to the side of the layer involved, measured from the side of the specimen on which the primary beam is incident.

b) A transmission pinhole photograph is made of a sheet of aluminum 0.5 mm thick with Cu $K\alpha$ radiation. Consider only the 111 reflection which occurs at $2\theta = 38.4°$. Imagine the sheet to be divided into four layers, the thickness of each being equal to one-fourth of the total thickness. Calculate T for each layer.

14-6 A transmission pinhole pattern is made with Co $K\alpha$ radiation of an iron wire having an almost perfect [110] fiber texture. The wire axis is vertical. How many high-intensity maxima will appear on the lowest-angle 110 Debye ring and what are their azimuthal angles on the film?

14-7 An electroplated layer of copper on sheet steel is examined in a back-reflection pinhole camera with Cu $K\alpha$ radiation incident at right angles to the sheet surface. Assume the copper has a fiber texture with the fiber axis $[uvw]$ scattered by an angle β in every direction about the sheet normal. How large must β be for the 420 Debye ring (see Table 4-2) to appear on the film if the fiber axis $[uvw]$ is (a) [110], (b) [100]?

14-8 Consider the diffraction geometry for $\alpha = 0$ in the transmission method for determining preferred orientation and for $\alpha = 90°$ in the reflection method. Let t_{inf} be the infinite thickness required in the reflection method, and assume t_{inf} is that thickness which would diffract 99 percent of the intensity diffracted by a specimen of truly infinite thickness. Let t_{opt} be the optimum thickness for the transmission method.

a) Show that $t_{inf}/t_{opt} = 2.30 \tan \theta$.

b) If the thickness t of a transmission specimen is 2topt, by how much is the diffracted intensity decreased?

14-9 On a stereographic projection parallel to the surface of a rolled sheet, show (a) the positions of the (110) poles, represented by small ellipses, for the ideal orientation $\{111\}\langle 110\rangle$, including the positions due to reflection symmetry, and (b) the lines showing the positions of the (110) poles for a $\langle 111\rangle$ fiber texture, with the fiber axis normal to the plane of the sheet. Compare your result with the experimental (110) pole figure for low-carbon sheet steel in Fig. 14.22.